

# UNIVERSITY OF TWENTE.

## Radboudumc

University of Twente  
Magnetic Detection & Imaging (MD&I)  
Radboud UMC  
Neurochirurgie & Radiologie

## RF Heating Mitigation around a DBS lead at 3T

Wiesje Roskamp

Biomedical Engineering

M.Sc.Thesis

September 2022 - May 2023

---

**Committee:**

Dr. ir. Wyger M. Brink  
Dr. ir. Kristian Overduin  
Dr. ir. Marinette van der Graaf  
Dr. drs. Saman Vinke

**Head of committee:**

Prof. dr. ir. Bernard ten Haken

**External member:**

Prof. dr. ir. Kees H. Slump

University of Twente  
P.O. Box 217  
7500 AE Enschede  
The Netherlands

---



# Acknowledgment

First of all, I would like to thank Wyger Brink, Kristian Overduin, Marinette van der Graaf, and Saman Vinke for their supervision during my master thesis assignment. The meetings have taught me to take a critical evaluation of my research outcomes. The insights and knowledge acquired regarding MRI and RF coupling proved invaluable in explaining processes and determining future steps. Furthermore, I am grateful for the opportunity you provided me to submit an abstract to the ISMRM 2023 Benelux Conference. And to top it off, we were allowed to present this interesting project.

I would like to express my gratitude to Wyger for giving me the opportunity to conduct my thesis assignment externally. Next to this, your feedback and the discussions we engaged in served to enhance my enthusiasm for the field of MRI. I would also like to extend my thanks to Marinette for her invaluable assistance in conducting the measurements. Additionally, I could always rely on your expertise and guidance for any questions that arose. Next to this, I would like to extend my gratitude to Kristian for his critical perspective and insightful contributions in analysing and explaining the processes encountered throughout this project.

Moreover, I am also grateful to the Vinke Lab group for the pleasant experiences I had during my time in this department. The availability of colleagues to address my questions and the knowledge I gained through the weekly meetings greatly contributed to my understanding of various research areas within the DBS field. Additionally, observing the intricacies of the publication and peer-review process was highly informative. Special recognition is extended to Saman for providing me with valuable medical insights about the DBS procedure. I would also like to thank Ashok Selvaraj for assisting me in preparing my phantom, and Dirk Loeffen for offering his assistance during measurements.

I am deeply grateful to Andor Veltien for designing my measurement setup. Your expertise and ideas were instrumental in its success. I also wish to express my gratitude to Bennie Ten Haken and Kees Slump for generously dedicating their time and providing valuable feedback during the course of my graduation project. Additionally, I would like to acknowledge the support of my family and friends throughout this project.

Finally, I am delighted that Camille Speybroeck will be carrying forward this project. I want to wish you the best of luck in the upcoming steps you will take within this project.



# Summary

The aim of this study is to propose a new method for mitigating the radiofrequency (RF) heating that occurs around a deep brain stimulation (DBS) lead during 3T MRI scans, in a reliable manner. This can be achieved by reducing the induced current at the shaft of DBS lead through the use of safe RF excitation settings. The extent of RF coupling between the MR scanner and the DBS lead is highly dependent on the geometry of the implanted DBS system of the patient, thus highlighting the need for a patient-specific method. Several patient-specific methods have been documented in literature [1]. The technical principles of these methods in determining a safe RF excitation pattern has been established; however, their clinical applicability remains limited due to a high degree of user dependency.

To determine safe RF excitation pattern, or implant friendly (IF) mode, low-SAR 2D Gradient Echo Sequence (GRE) calibration images were acquired for both transmit channels of the MRI scanner. The induced current from both pre-scans was then determined by utilizing the position of transmission RF magnetic field (Tx) null location relative to the DBS lead. An agar phantom that included a DBS lead connected with an implantable pulse generator (IPG) was used as the measurement setup. To improve the reliability and robustness, we purposed a model-based fitting approach that involved using a quasi-static RF field model to simulate the local  $B_1^+$  perturbation caused by a DBS lead. The reduction of RF heating was validated by real-time temperature measurements and the visual inspection of the image quality measured with T2 weighted turbo spin echo (TSE) MRI sequence.

The IF excitation patterns determined using the manual and model-based approach resulted in similar mitigation of the Tx-null artefact and RF heating around the tip of the DBS lead. However, the manual approach showed dependence on the user. It was observed that when the amplitude of the incident  $B_1^+$  field was added in the induced current calculation, the temperature rise was slightly lower. Moreover, the comparing of the IF modes with the quadrature excitation pattern resulted in a significant reduction of the RF heating and the Tx-null at the shaft of the DBS lead when utilizing the IF modes.

In this study, it is shown that a model-based approach provides a comparable mitigation of the RF heating as compared to the manual approach, while offering a more reliable and robust outcome and eliminating user dependency. Therefore, it holds promise for potential integration of this method into clinical practise. Nonetheless, further research is required to investigate the effect of oblique orientation of a DBS lead and to optimize and automate the model-based approach by varying the size of the masks, using a different resolution of the GRE pre-scans or by addition the  $B_1^+$  amplitude in the quasi-static RF field model. A phantom with two leads could also be considered for further investigation.



# Samenvatting

Het doel van deze studie is het introduceren van een nieuwe methode om radio frequente (RF) opwarming die optreedt rondom een geïmplanteerde diepe hersenstimulatie (DBS) draad tijdens een 3T MRI scan op een betrouwbare manier te beperken. Dit kan worden bereikt door de geïnduceerde stroom bij de schacht van het DBS draad te verminderen door het gebruik van veilige RF excitatie instellingen. De mate van RF koppeling tussen de MR scanner en het DBS draad is sterk afhankelijk van de geometrie van het geïmplanteerde DBS systeem in de patiënt, daarom is er behoefte aan een patiënt specifieke methode. In de literatuur zijn meerdere onderzoeken beschreven die gebruik maken van patient specifieke methode [1]. De technische principes van deze methodes om een veilig RF excitatie patroon te bepalen zijn beschreven, echter kan op dit moment zo'n methode nog niet geïntegreerd worden in de kliniek door de grote mate van gebruikersafhankelijkheid.

Om het veilige RF excitatie patroon, oftewel de implantaat vriendelijke (IF) modus, te bepalen werden lage-SAR 2D Gradient Echo Sequentie (GRE) kalibratiebeelden verkregen voor beide transmissie kanalen van de MRI scanner. De geïnduceerde stroom werd bepaald voor beide pre-scans door gebruik te maken van de positie van de nul locatie van het transmissie RF magneetveld (Tx) ten opzichte van het DBS draad. In dit onderzoek is een agar fantoom met een DBS draad die gekoppeld is aan een implanteerbare puls-generator (IPG) als meetopstelling gebruikt. Om de betrouwbaarheid en robuustheid te verbeteren werd er een methode gebruikt die gebaseerd was op het simuleren van een quasi-statisch RF veldmodel van de lokale  $B_1^+$  verstoring die veroorzaakt wordt door een DBS-draad. De vermindering van RF verwarming werd gevalideerd door het verrichten van real-time temperatuurmetingen en visuele inspectie van de gemeten beeldkwaliteit met T2-gewogen turbo spin echo (TSE) MRI sequentie.

De IF excitatie patronen die bepaald zijn met de handmatige en model gebaseerde aanpak resulteerden in vergelijkbare vermindering van het Tx-null artefact en RF opwarming rond de tip van het DBS-draad. De handmatige aanpak bevatte echter een mate van gebruikersafhankelijkheid. Er werd daarnaast geconstateerd dat wanneer de amplitude van het invallende  $B_1^+$  veld werd toegevoegd aan de berekening van de geïnduceerde stroom, de temperatuurstijging iets lager werd. Bovendien resulteerde de IF modi in vergelijking met het kwadratuur excitatie patroon in een aanzienlijke vermindering van de RF opwarming en het Tx-null artefact rondom de schacht van het DBS draad.

In deze studie is aangetoond dat een model gebaseerde methode een vergelijkbare vermindering van de RF opwarming oplevert in vergelijking met de handmatige benadering. Echter is het resultaat verkregen met de model gebaseerde methode betrouwbaarder, robuuster en nauwelijks afhankelijk van de gebruiker. Daarom biedt deze methode een mogelijkheid voor het integreren in de kliniek. Niettemin is verder onderzoek nodig, voordat deze methode geïntegreerd en volledig geautomatiseerd kan worden. Voorbeelden hiervan zijn het onderzoeken van het effect van een schuine oriëntatie van een DBS draad en het optimaliseren van de model gebaseerde aanpak door de grootte van de maskers te variëren, een andere resolutie van de GRE pre-scans te gebruiken of door de  $B_1^+$  amplitude in het quasi-statische RF-veldmodel toe te voegen. Voor verder onderzoek kan ook een fantoom met twee draden overwogen worden.

# Contents

<b>Acknowledgment</b>	<b>iii</b>
<b>Summary</b>	<b>v</b>
<b>Samenvatting</b>	<b>vii</b>
<b>Abbreviation List</b>	<b>xi</b>
<b>1 Introduction</b>	<b>1</b>
<b>2 Theory</b>	<b>3</b>
2.1 Induced current . . . . .	3
2.2 The $B_1^+$ distribution in DBS lead . . . . .	4
2.3 Safety . . . . .	6
2.3.1 Temperature probe . . . . .	6
<b>3 Materials &amp; Methods</b>	<b>7</b>
3.1 Materials . . . . .	7
3.1.1 DBS lead . . . . .	7
3.1.2 Phantom . . . . .	7
3.1.3 IPG setting . . . . .	8
3.1.4 Temperature thermometers . . . . .	8
3.2 Methods . . . . .	9
3.2.1 MRI measurements . . . . .	9
3.2.2 Manual approach . . . . .	10
3.2.3 Model-based approach . . . . .	11
3.2.4 Quantitative induced current calculation . . . . .	12
<b>4 Results</b>	<b>13</b>
4.1 Manual approach . . . . .	13
4.2 Model-based approach . . . . .	15
4.3 Quantitative induced current calculation . . . . .	16
4.4 Assessment of methods . . . . .	16
<b>5 Discussion</b>	<b>19</b>
5.1 Discussion . . . . .	19
5.2 Limitations . . . . .	20
5.3 Future recommendations . . . . .	21
5.4 Future perspectives . . . . .	22
<b>6 Conclusion</b>	<b>23</b>
<b>Bibliography</b>	<b>24</b>
<b>A Derivation of <math>B_{sct}</math> equation</b>	<b>29</b>

---

<b>B Safety restrictions DBS lead</b>	<b>31</b>
<b>C Additional information scan protocol</b>	<b>33</b>
<b>D Temperature rise in background</b>	<b>35</b>



# Abbreviation List

$B_0$	-	Static Magnetic field
$\mathbf{B}_1$	-	Radio Frequency Magnetic field vector
$B_1^+$	-	Transmit Magnetic Radio Frequency field
$B_{1,inc}^+$	-	Incident Radio Frequency Magnetic field of MRI scanner
$B_{1,rms}^+$	-	Root-mean-square of Transmit Radio Frequency Magnetic field
$B_{1,sct}^+$	-	Scattered Radio Frequency Magnetic field of DBS lead
BG	-	Background
Ch1	-	Channel 1 of the body coil of the 3T MRI scanner
Ch2	-	Channel 2 of the body coil of the 3T MRI scanner
CT	-	Computed Tomography
DBS	-	Deep Brain Stimulation
EM	-	Electromagnetic
FOV	-	Field-of-View
GRE	-	Gradient Echo
$I_{sct}$	-	Induced Current
IF	-	Implant Friendly
IPG	-	Internal Pulse Generator
MRI	-	Magnetic Resonance Imaging
OR	-	Operation Room
RF	-	Radio Frequency
ROI	-	Region of Interest
SAR	-	Specific Absorption Rate
SI	-	Signal Intensity
SNR	-	Signal to Noise ratio
Tx-null	-	Transmission RF magnetic field null artefact
TE	-	Echo Time
TR	-	Repetition Time
T2_TSE	-	T2 weighted turbo spin echo
UMC	-	University Medical Center



# Introduction

Deep brain stimulation (DBS) is a therapy that involves the implantation of electrodes for electrical stimulation of the brain and can be used to ease symptoms of Parkinson’s disease, tremor, or dystonia [2]. Accurate placement of the leads in the target region is crucial, as misplacements can result in a diminished function of the DBS system, and thereby can have a negative impact on the effectiveness of the therapy. Side-effects such as depression, ocular deviation, and headaches may arise as well [3].

At the Radboud University Medical Center (UMC), a pre-operative magnetic resonance imaging (MRI) 3T scan is used to establish the target location of the DBS lead, its placement is evaluated and confirmed through post-operative computed tomography (CT) imaging. While this image modality provides useful information, it presents some limitations, such as a low soft tissue contrast, exposure to ionizing radiation, and image artefacts around the DBS lead [4, 5]. Although MRI has the potential to improve these limitations, post-operative MR imaging poses safety concerns due to potential localized heating of tissues surrounding the DBS lead [3, 6]. The observed phenomenon can be attributed to the interaction between the incident radiofrequency (RF) field and the localized RF field of the wire, which results in the induction of a current. The enhancement of the RF field in the vicinity of the lead tip can cause thermal damage and, ultimately, tissue necrosis in the brain. Unfortunately, several cases have been reported detailing (permanent) injuries when scanning patients with an implanted DBS lead with MRI [7, 8, 9]. Additionally, pronounced image artefacts may also arise due to perturbation in the RF magnetic field ( $B_1^+$ ) induced by the DBS lead [10].

Due to the potential risk of RF heating, MR imaging with DBS implants is often compromised. The majority of DBS leads are MR conditional at 1.5T and impose conservative restrictions on sequence parameters such as flip angle or repetition time, while only a few leads are labeled for use in 3T MRI. Establishing safety labels for higher magnetic field strengths is a complex process, as RF field enhancement can become more prominent presence around the DBS lead and potentially result to local heating. Consequently, manufacturers place the responsibility on the user to avoid potential hazards. Despite these concerns, higher magnetic field strengths offer several advantages, such as higher signal-to-noise ratio (SNR), and an improved image quality [11]. Some studies even suggest that higher field strengths can cause similar or even less local heating [6, 12, 13]. In addition, clinicians in the Radboud UMC have expressed a preference to switch the post-operative CT imaging step to post-operative MR imaging, given its potential for intra-operative confirmation, increased efficiency and improved patient and clinician experiences. The current and proposed operation programs are illustrated in Figure 1.1.

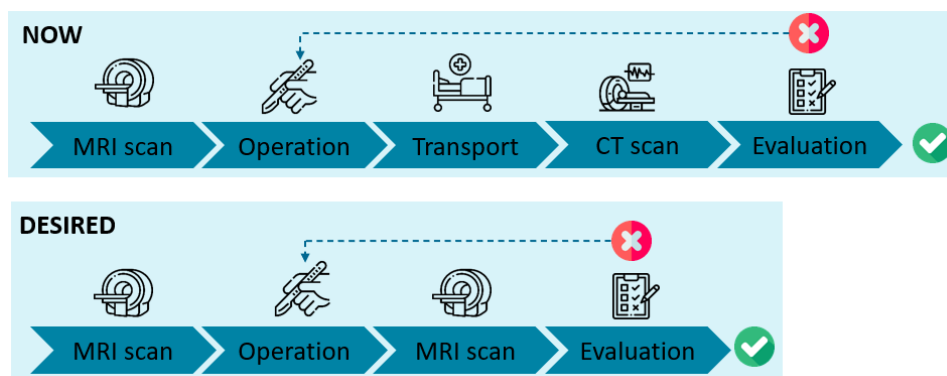


**Figure 1.1:** Current and desired DBS operation procedure at Radboud UMC where 3T MRI scanner is available at OR.

Various approaches to address mitigation of the RF heating have been proposed in literature. Modifications to the DBS system can be made by changing the design of the coiled wires [14, 15, 16] or altering the wire materials [17]. Despite the promising results from these studies, implementing these approaches lead to a more intricate and expensive design of the DBS system. Other factors affecting RF coupling are the trajectory and length of the DBS lead [6, 18, 19, 20, 21]. The extent of coupling is highly dependent on the geometry of the implanted DBS system of the patient.

An alternative strategy involves the manipulation of the local specific absorption rate (SAR) through steering of the transmit coil of the MRI scanner [22]. The utilization of a 3T scanner can lead to pronounced  $B_1^+$  non-uniformities as the RF wavelength approaches the dimensions of the human body [23]. This can result in issues such as inhomogeneous excitation and diminished image quality. RF shimming, which involves adjusting the transmit channel(s) of a 3T scanner, can be utilized to address these challenges. RF shimming is a well-established technology that has been employed in numerous studies while maintaining flip angle homogeneity. It has been shown that dual-drive excitation can alter the SAR, allowing for a reduction in temperature around metallic devices [19, 3, 24, 25]. Another option is the use of a linearly polarized rotatable birdcage transmitter to steer the plane in which the SAR is zero [18, 26].

Despite these attempts to address and mitigate RF coupling to implanted DBS systems, a universally accepted method that ensures safe scanning in all patients with an implanted DBS lead at 3T MRI, has yet to be established. The RF coupling is highly dependent on the geometry of the DBS system in the patient. As such, the development of a patient-specific method for safely scanning DBS patients with a 3T MRI scanner is highly desirable. One particular study presented a patient-specific method to derive RF excitation settings that mitigate RF heating [1]. This study demonstrates potential for the integration of an off-label method into clinical practice. Prior to performing this, an improved understanding of the phenomenon of RF coupling with DBS lead is necessary. Further testing and validation are imperative. The method's robustness and reliability need improvement to reduce user dependency in this process, thereby enabling its integration into clinical practice.

In this work, the aim is to propose a method for predicting safe RF excitation settings in a patient-specific manner when a DBS implant is present. We follow the approach of [1] using low-SAR 2D gradient echo (GRE) pre-scan images made with 3T MRI. The RF settings that cancel the RF induced current on the DBS implant are determined by estimating the induced current on the DBS lead based on the pre-scan calibration data [19]. The following research question will be addressed: *"How can GRE pre-scans acquired with a 3T MRI scanner be utilized to predict the induced current at the shaft of a DBS lead and determine safe RF excitation settings in a reliable manner?"*

Related sub aims in this research are:

- Gain insight into the RF coupling phenomenon with a DBS lead.
- Confirm that the safe RF excitation settings reduces RF heating around the DBS tip.
- Compare the manual and semi-automated approaches for determining safe RF excitation settings.

To improve the robustness and reliability, we propose a model-based fitting approach to derive the induced current around a DBS lead. A quasi-static RF field model simulate the local  $B_1^+$  perturbation caused by the DBS current. The study investigates an agar phantom that incorporates a DBS lead and IPG in the experimental setup. The effectiveness and safety of the proposed methods are evaluated by quantifying the temperature rise near the tip of the DBS lead for both the safe RF excitation pattern and conventional quadrature excitation pattern.

# Theory

In the context of MRI, the underlying physics involve the interaction of two independent magnetic fields with a nuclear spin system, namely the static magnetic field denoted by  $B_0$  and the transmit RF field represented by  $B_1^+$ , with a nuclear spin system. The  $B_1^+$  field is typically applied perpendicular to the  $B_0$  field, resulting in a change in the direction of magnetization. This adjustment ultimately produces a detectable RF signal [27]. Furthermore, the application of the transmit RF field is associated with the induction of currents in conductive tissues, leading to energy absorption and tissue heating [3].

## 2.1 Induced current

The transmitted RF field can couple with the conductive DBS leads which results in the induction of a current [3, 28]. This current can enhance the electric field intensity in the vicinity of the tip of the lead, leading to high local values of specific absorption rate (SAR). This phenomena is commonly referred to as the ‘antenna effect’ [18, 19]. The amplifications of SAR values can produce local RF heating of the brain tissue, which may ultimately cause thermal tissue damage [3, 18, 19, 28]. In Figure 2.1, the local SAR enhancement resulting from RF coupling can be observed at the tip of lead.

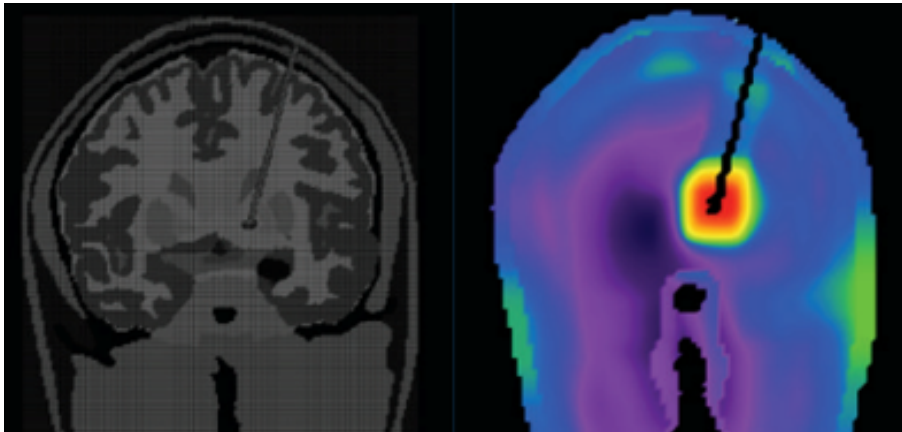


**Figure 2.1:** An anatomic model (left) and the local SAR enhancement around a DBS lead (right) [29].

To ensure safe scanning of a DBS system in a 3T MRI scan, it is necessary to minimize the induced current to zero. Ohmic losses can reduce the current in the surrounding tissue, thereby leading to a decrease in SAR.

Apart from the thermal effects caused by RF field enhancement, the current induced on the shaft of the DBS lead will also give rise to a perturbation in the  $B_1^+$  field, which in turn can lead to an image artefact [6, 18]. This artefact can typically be observed around the DBS lead and can pose challenges in accurately assessing the position of the implanted lead. It has been demonstrated in literature that there exists a correlation between the image artefact in the transmit RF field and the local SAR values [19]. The location of the artefact can be utilized to describe and subsequently mitigate the RF field enhancements in the vicinity of the DBS lead [1].

## 2.2 The $B_1^+$ distribution in DBS lead

In order to gain a more comprehensive understanding of the phenomenon that leads to the formation of an artefact around a DBS lead, further elucidation is required on the manifestation of this image artefact. This can be achieved by examining the signal intensity (brightness) of the pre-scans. In this study a multi-channel receiver array is used to acquire the low flip angle GRE images. The signal intensity ( $SI$ ) can be expressed as a combination of the receiver sensitivity and transmitter sensitivity detected at the vicinity of the DBS lead. Each component is formed by the combination of the magnetic field produced by the current that is induced on the DBS lead and the incident field ( $B_{1,inc}^+$ ). The  $SI$  of the  $m$ th receiver coil is given by the following equation [1]:

$$SI_m \sim \underbrace{\left( B_{1,inc,m}^- - (\text{icos}(\phi) + \sin(\phi)) \frac{\mu_0 I_m^r}{4\pi r} \right)}_{\text{receiver}} \cdot \underbrace{\left( B_{1,inc}^+ + (\text{icos}(\phi) - \sin(\phi)) \frac{\mu_0 I^t}{4\pi r} \right)}_{\text{transmitter}} \quad (2.1)$$

In this equation,  $\mu_0$  represents the magnetic permeability in vacuum and  $I$  denotes the induced current on the wire obtained during receiving and transmission. The radial distance between the wire and the desired observation point is denoted with  $r$ . The radial distance has to be perpendicular to the wire. The  $\phi$  denotes the scalar with respect to the x-axis of the magnetic field. By setting this equation equal to zero, two solutions for the null-locations can be derived: the receiver null location (Rx-null) and the transmitter null location (Tx-null). While the Tx-null is located at the same position for all elements, the Rx-null varies for each receiver element [1].

In a sum-of-squares reconstruction of Equation 2.1 this results in the elimination of the Rx-null location in the image. This phenomenon can be explained by the following equation, which describes the  $SI$  around the DBS lead [1]:

$$SI \sim \sqrt{\sum_m \left| \left( B_{1,inc,m}^- - (\text{icos}(\phi) + \sin(\phi)) \frac{\mu_0 I_m^r}{4\pi r} \right)^2 \right.} \cdot \left( B_{1,inc}^+ + (\text{icos}(\phi) - \sin(\phi)) \frac{\mu_0 I^t}{4\pi r} \right) \quad (2.2)$$

In this equation, only one null location is obtained, namely the Tx-null which is only dependent on the transmit RF field and the induced current. The Tx-null is the location where the  $B_{1,inc}^+$  and the magnetic field of the DBS lead field ( $B_{1,sct}^+$ ) cancel each other out, resulting in a total transmit RF field of zero [30].

The total transmit RF field distribution can be expressed as the sum of the incident circularly polarized RF transmit magnetic field generated by the transmit body coil of the scanner ( $B_{1,inc}^+$ ) and the scattered RF magnetic field generated by the electric currents induced on the DBS lead ( $B_{1,sct}^+$ ) [10, 31]:

$$B_{1,tot}^+ = B_{1,inc}^+ + B_{1,sct}^+ \quad (2.3)$$

The electric current in the wire produces a magnetic field which is circular symmetric and centered on the wire. The magnitude of the scattered magnetic field,  $\mathbf{B}_{sct}$ , at any distance away from the wire can be derived from the analytical field solution that corresponds to an infinite wire. This equation can be derived from the Biot-Savart Law. The derivation can be found in Appendix A. The following Equation is obtained [10, 30]:

$$\mathbf{B}_{sct} = \frac{\mu_0 \cdot I_{sct}}{2\pi \cdot r} \cdot \hat{\phi} \quad (2.4)$$

In this equation, the  $\mathbf{B}_{sct}$  and  $r$  are inversely proportional to each other. The vector  $\hat{\phi}$  is the cylindrical unit vector of the magnetic field. And the  $I_{sct}$  denotes the induced current on the wire. The fraction presented in this Equation is commonly referred to as the magnitude of the magnetic field scattered by the wire, which is denoted as  $B_\phi$ . In order to mitigate the RF field enhancement and the subsequent emergence of

the Tx-null artefact, the Tx-null will be employed as an observation point.

In clinical settings, DBS leads are frequently implanted at oblique angles. Consequently, it becomes necessary to include an additional  $\frac{1}{\cos(\theta)}$  term, where  $\theta$  denotes the angle between the conventional MRI scanner coordinate system (i.e., the laboratory frame) and the new coordinate system. In this study, the DBS lead is situated in the laboratory frame (along the  $B_0$  field), leading to  $\cos(0) = 1$ .

The induced current on a DBS lead in Equation 2.4 can be described with the following Equation [1]:

$$|I_{sct}| = \frac{|B_{1,inc}^+| 4\pi r_0}{\mu_0}, \angle I_{sct} = \phi_0 \quad (2.5)$$

The radial distance between the wire and the Tx-null location is denoted as  $r_0$ , and  $\phi_0$  represents the geometric angle of the Tx-null. An example of the image artefact around a DBS lead is illustrated in Figure 2.2.

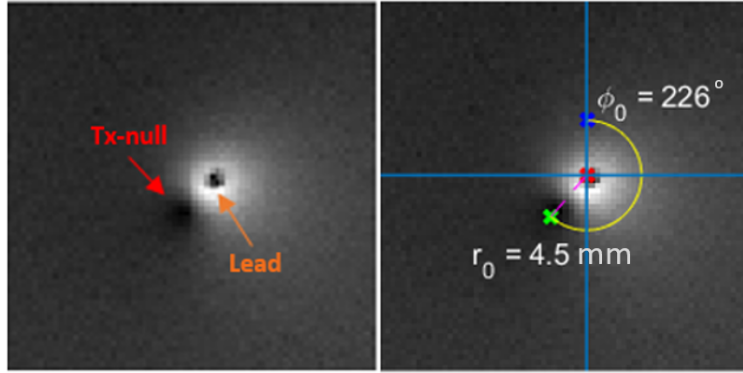


**Figure 2.2:** Low-SAR 2D GRE pre-scan made with excitation pattern of calibration scan 1. Left indicate the position of the DBS lead and the Tx-null. On the right, the values found for  $r_0$  and  $\phi_0$  are indicated.

In this study,  $B_1$  values are represented as complex numbers and employs circularly polarized components of RF magnetic field for both excitation and reception purposes. The transmitted circularly polarized RF magnetic field,  $B_1^+$ , can be ascertained through the utilization of the subsequent equation, wherein  $B_x$  and  $B_y$  symbolize the magnetic x- and y-components respectively, as measured along the laboratory frame of the MRI scanner [32]:

$$B_{1,sct}^+ = \frac{B_{x,sct} + iB_{y,sct}}{2} \quad (2.6)$$

Assuming that the  $B_\phi$  field runs parallel to the  $B_0$  field, the two components can be ascertained from  $B_1$  through utilization of the following equation [32]:

$$B_{x,sct} = -B_\phi \cdot \sin(\phi) \quad (2.7)$$

$$B_{y,sct} = B_\phi \cdot \cos(\phi) \quad (2.8)$$

Through the substitution of Equation 2.7 and 2.8 into Equation 2.6, the resulting equation may be derived: [10, 1, 30]:

$$B_{1,sct}^+ = \frac{i\cos(\phi) - \sin(\phi)}{2} \cdot B_\phi \quad (2.9)$$

Now the determination of  $B_{1,sct}$  can be carried out. For  $B_{1,sct}$ , Equation 2.4 can be incorporated into the aforementioned equation, yielding the ensuing outcome, [30]:

$$B_{1,sct}^+ = (i\cos(\phi) - \sin(\phi)) \cdot \frac{\mu_0 \cdot I_{sct}}{4\pi \cdot r_0} \quad (2.10)$$

The  $B_{1,tot}^+$  can be expressed by the summation of Equation 2.10 and  $B_{1,inc}^+$ . The determination of  $B_{1,inc}^+$  can be attained through the utilization of the complex values of the transmit channels of the MR scanner. This gives the following expression:

$$B_{1,tot}^+ = B_{1,inc}^+ \cdot (\cos(\phi) - \sin(\phi)) \cdot \frac{\mu_0 \cdot I_{sct}}{4\pi \cdot r_0} \quad (2.11)$$

This Equation can be used for the quasi-static RF field model. The calculation of the induced current in this equation can be determined by utilizing Equation 2.5. Equation 2.11 is also used in Equation 2.1 as the transmitter component of the signal intensity.

## 2.3 Safety

MRI scans of patients with a DBS system require mandatory safety restrictions due to potential risks [19]. These safety thresholds are typically defined in terms of the whole body and/or head SAR or root-mean-square (rms) value of the  $B_1^+$  component of the magnetic field. While the  $B_{1,rms}^+$  value depends on the pulse sequence design and is not affected by the patient [33], the SAR values are influenced by the patient's anatomy and presence of implants. Actual SAR and  $B_{1,rms}^+$  levels can be reduced by the number of slices/echoes or the flip angle, or by increasing the repetition time (TR) [34]. A summary of the safety restrictions of the measured DBS lead is presented in Appendix B Table B.1.

### 2.3.1 Temperature probe

The safety of the proposed method is assessed by measuring the temperature rise around the DBS lead using fiber-optic probes positioned around the contacts of the lead. The temperature change is measured in real-time, and the probes must be positioned carefully to capture the maximum heating. Typically, studies that involve the assessment of real-time heating resulting from the measurement of DBS system components in an MRI scanner utilize a safety limit of 1 or 2° C [34, 35, 36, 37]. In this study, a safety limit of 2° C will be adopted.

Previous studies have shown that the maximum heating occurs at the shaft of the contacts, specifically at a distance of 0.5 to 1 mm [16, 30]. In order to accurately measure this effect, it is recommended to place the temperature probes as close as possible to the contacts, as depicted in Figure 2.3. Sadeghi-Tarakameh et al [30], investigated four different contacts and found similar heating profiles over time, as well as comparable peak temperatures.

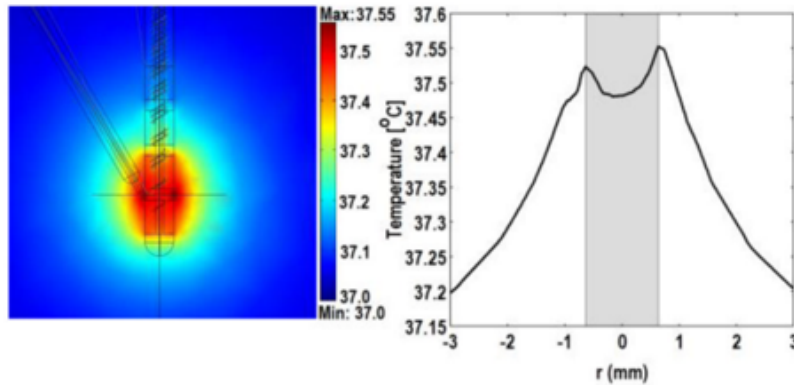


**Figure 2.3:** The heating around a DBS lead. On the left the temperature increase is illustrated in color. On the right, a cross sectional view displays the ambient temperature [16].

# Materials & Methods

In this study, two distinct methodologies are employed to ascertain safe RF excitation patterns. Specifically, a phantom setup, which includes a DBS lead, IPG, and temperature probes, was used to carry out the investigation. First, a comprehensive description and illustration of the materials utilized in this study is presented. Following this, the two methodologies employed for the computation of the induced current and safe RF excitation patterns is elaborated upon.

## 3.1 Materials

### 3.1.1 DBS lead

This study utilized a Boston Scientific Cartesia Directional lead (DB-2202-30), to evaluate the method. This specific lead comprises two types of contact points: directional and ring electrodes. Directional electrodes cover a smaller surface area than the ring electrodes and are arranged in a circular formation consisting of three electrodes. When combined with the ring electrode, which encompasses the two outer circular contacts, this arrangement yields a DBS lead with a total of eight electrodes. In addition, the DBS lead contains a radio-opaque marker to establish the orientation of these contacts during CT imaging. The configuration of the lead is displayed in Figure 3.1.

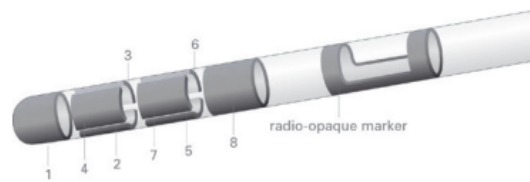


**Figure 3.1:** Boston Cartesia Directional lead DB-2202-30 [38].

### 3.1.2 Phantom

The phantom employed in this study, measuring 39x29x26 cm, was designed to mimic a clinical scenario in which a patient is in a lateral decubitus position. This phantom was prepared using an agar gel solution (2g/L Sodium Chloride (NaCl) and 30 g/L Agar) which imitates the electrical properties of human brain tissue. The phantom was utilized to assess the impact of the DBS lead, when fully cast in agar, on the method with multiple temperature probes placed at various locations to draw conclusion about the safety of the method. This phantom included a DBS lead, an IPG, and three temperature probes positioned at the IPG, tip of the lead and background, with the final temperature probe serving as a reference measurement. The phantom featured poles with holes drilled at different heights, enabling users to alter heights and distances of the wires. The measurement setup of this phantom is depicted in Figure 3.2.

In an effort to simulate a typical DBS patient configuration, the DBS lead wire was positioned in accordance with a left DBS lead placement. Subsequently, both the DBS lead wire and the temperature probes were embedded in agar and the lead was connected to the IPG. The tip of the DBS lead was centrally located in the phantom at a height of 5 cm (measured from the bottom of the box), with the DBS lead extending along the skull and ear towards the shoulders. At the bend of the lead (along ear), the height was changed. From there, the lead ran straight towards the IPG. The temperature probes were strategically positioned to allow for accurate measurements, with the background probe positioned at a height of 4 cm (measured from the bottom of the box).

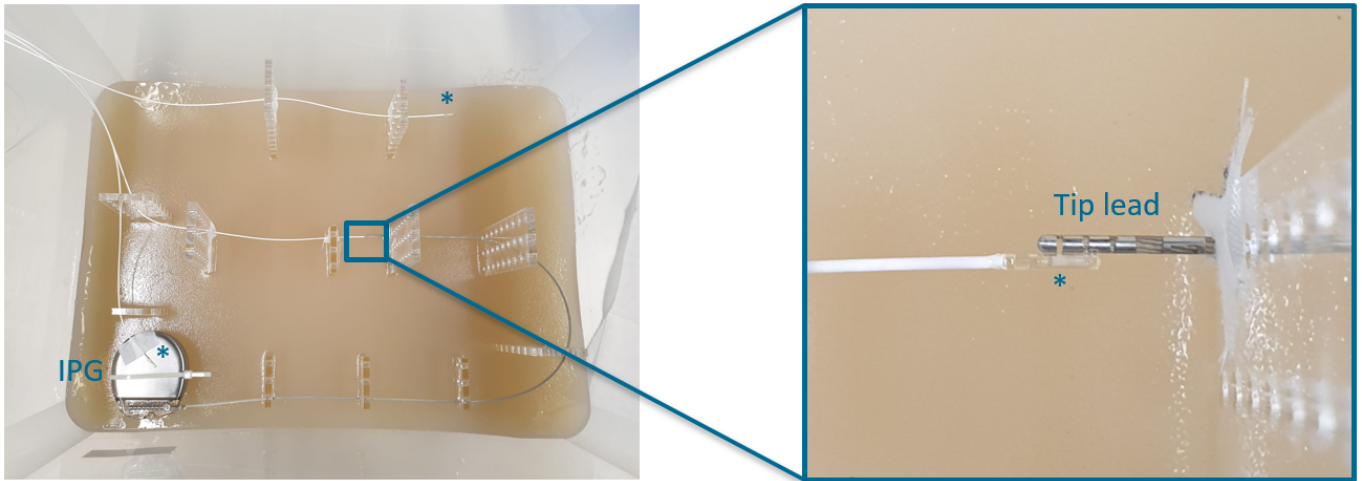


**Figure 3.2:** The configuration of the utilized phantom. In this phantom a DBS lead connected with an IPG are molded into the phantom. The temperature probes are indicated with \*.

### 3.1.3 IPG setting

This study employed the Vercise Gevia rechargeable battery for the experimental setup. The IPG was positioned outside of the agar medium. When a DBS patient undergoes a 1.5T MRI scan, the IPG is configured to operate in the 'MRI Modus', which is a safety mode that has been verified by the manufacturer for conducting MRI scans on a DBS system. In this study, the IPG was manually configured into this mode by implementing the following steps:

- Impedance test: This test was used to check that the DBS system is intact and that there is no kink in the wiring.
- Set amplitude to zero
- Stimulation off



**Figure 3.3:** The Vercise Gevia rechargeable battery [39].

### 3.1.4 Temperature thermometers

The temperature was monitored in real-time using a fiber-optic temperature thermometer. In the measurement setup the 4-channel OpSens AccuSens thermometer with a resolution of 0.01 °C was used. This thermometer is depicted in Figure 3.4.



**Figure 3.4:** The OpSens AccuSens thermometer used for real-time temperature measurements [40].

## 3.2 Methods

Two approaches were utilized to calculate the induced current and predicted safe RF excitation settings, also called the implant friendly (IF) modes. The first approach involved manual determination of the magnitude and phase of the induced current using the Tx-null and lead location in a GRE pre-scan. The other approach employed a model-based fitting procedure using Matlab (R2020a, Mathworks, NA). In this approach, a quasi-static RF field model was used to describe the  $B_1^+$  perturbation caused by the DBS current. The calculated induced current and the  $B_1^-$  field were used as inputs for this model, which resulted in a GRE image as output.

### 3.2.1 MRI measurements

In this study, all measurements were acquired utilizing a Siemens Skyra 3T system located in the OR of the Radboud UMC. The phantom was positioned head-first supine orientation, with the tip of the lead indicated at the magnet isocenter in the scanner. Throughout the majority of the measurements, a simulated 53-year-old individual, weighing 80 kg and standing 180 cm tall, was used as the "patient". These settings were employed to calculate the predicted safety values expressed in SAR. The RF pulses were transmitted with the system's body coil, and received with an 18-channel body coil and the spine coil. The phantom was placed in the center of the spine coil.

A low-SAR 2D GRE pre-scan (flip angle=30°, TR=200 msec, TE=3.80 msec, 0.5x0.5x5mm, FOV= 25cm x 25 cm, acquisition time = 31 sec, GRAPPA acc. N=4), was obtained. The distinct excitation patterns were scanned using the "patient specific" RF shimming setting of the RF transmit channels, Channel 1 (Ch1) and Channel 2 (Ch2) (Table 3.1). The pre-scans were conducted perpendicular to the shaft of the DBS lead, positioned at a height of 3 cm seen from the tip. This height was chosen to avoid scanning GRE images at the electrodes. The determination of the slice position was achieved through the acquisition of a T2 weighted turbo spin echo (T2\_TSE) protocol (flip angle=160°, TR=11610 msec, TE=102 msec, 0.5x0.5x5mm, FOV= 25cm x 25 cm, acquisition time = 69 sec, GRAPPA acc. N=1) in the transverse plane. The predicted SAR and  $B_{1,rms}^+$  values were calculated by the scanner and were recorded for both sequences. Details can be found in Appendix C Table C.1.

The safety of the predicted safe RF excitation pattern was confirmed through the real-time temperature measurements during a T2\_TSE sequence (flip angle=160°, TE=110 msec, 0.8x0.8x2mm, FOV= 21.8cm x 25 cm). The TR and number of slices were adjusted to achieve a predicted head SAR of around 100% for the IF mode. The IF mode was then compared with a commonly used quadrature mode (Table 3.1). Real-time temperature measurements were obtained from the thermometer during the scans, from which the temperature increase was determined.

Prior to the commencement of the subsequent temperature measurement, it was essential to allow the phantom to cool down to ensure standardization of the initial conditions for each measurement. The real-time whole body value (W/kg) must be observed to ensure a zero reading was obtained before proceeding to the next measurement. Moreover, temperature fluctuations observed on the thermometer display, must be taken into account and kept to a minimum to ensure accuracy. During the temperature measurement, it was crucial to note the safety values for the predicted head, and whole body SAR (%),  $B_{1,rms}^+$ , and RF power. These values facilitated an assessment of safety of the IF mode in comparison to the quadrature excitation pattern.

**Table 3.1:** The magnitude and phase values for the two transmit channels of the body coil of the scanner for the utilized excitation pattern.

Excitation pattern	Ch1	Ch2
Quadrature	0.71 $\angle 0^\circ$	0.71 $\angle 90^\circ$
Calibration scan 1	1 $\angle 0^\circ$	0 $\angle 0^\circ$
Calibration scan 2	0 $\angle 0^\circ$	1 $\angle 0^\circ$

### 3.2.2 Manual approach

The manual approach for determining a safe RF excitation pattern was based on manually selecting the DBS lead and Tx-null locations. Following the calculation of the relative induced current, the predicted IF mode was derived.

Initially, a localizer and slice position sequence was performed, after which the pre-scans of both transmit channels could be acquired using the determined slice position. The estimation of the induced current of both channels was achieved through the manual selection of the lead and Tx-null location in Matlab (R2020a, Mathworks, NA). The Tx-null location contained the information necessary to compute the induced current. The following steps should be undertaken:

1. Select ROI from original image where DBS lead and Tx-null are visible
2. Select DBS lead location
3. Select Tx-null location
4. Draw crosshair through the DBS lead location
5. Determine the  $r_0$  and  $\phi_0$  value
6. Calculate the induced current using Equation 2.5

Figure 2.2 depicted an example in which the DBS lead and Tx-null location were indicated by the orange and red arrow, respectively. The values for  $r_0$  and  $\phi_0$  could be determined manually by selecting two points (see right Figure 2.2 for values). Subsequently, the induced current for both transmit channels was computed using these values which were entered into Equation 2.5. The  $|B_{1,inc}^+|$  in this Equation was assumed to present a homogeneous field. Additionally, it was presumed that  $|B_{1,inc}^+|$  remains constant for both calibration scans, and was thus assigned a value of 1  $\mu\text{T}$ . To standardize the induced current calculation, the phase of the transmitted RF field was incorporated in Equation 2.5. The determined phase of the transmitted RF field was summed with the computed geometric angle of Tx-null ( $\phi_0$ ), which resulted in the following equation:

$$|I_t| = \frac{|B_{1,inc}^+| 4\pi r_0}{\mu_0}, \angle I_t = \phi_0 + \phi_{RF,field} \quad (3.1)$$

It is assumed that the transmitted RF field has a phase of zero for calibration scan 1, and a phase of 90 degrees for calibration scan 2. Upon determination of the induced current values for both channels, the IF mode could be derived as:

1.  $|a_1| = 1, \angle a_1 = 0^\circ$
2.  $|a_2| = \frac{|I_1|}{|I_2|}, \angle a_2 = 180^\circ - \angle \frac{I_2}{I_1}$

In this equation,  $a_1$  and  $a_2$  represent the magnitude and phase values to shim the transmitted  $B_1^+$  field to achieve the IF mode.

### 3.2.3 Model-based approach

A semi-automatic approach was utilized to reduce user dependency in the scanning procedure of DBS patients. Additionally, this technique could aid in achieving a more comprehensive understanding of the underlying processes involved in RF coupling. To simulate measured data effectively, it was imperative to include the transmission and reception component of the total  $B_1^-$  magnetic field, see Equation 2.1. The signal intensity of low flip angle GRE pre-scan was defined as:

$$SI = M_0 \sin(\gamma B_1^+ \tau) B_1^- \quad (3.2)$$

The  $B_{1,tot}^+$  was calculated using Equation 2.1, which utilizes the induced current values obtained through the manual approach. The initial maximum magnetization value,  $M_0$ , was obtained by fitting the simulation image to the measured image. The magnetogyric ratio,  $\gamma$ , and duration of the RF pulse,  $\tau$ , could be substituted by the flip angle. The  $B_{1,tot}^-$  field was considered constant, as explained in the Theory chapter, as the Rx-null was canceled out. Therefore, the influence of the  $B_1^-$  field was viewed as a constant factor in this simulation model. An illustration of this model is presented in Figure 3.5.

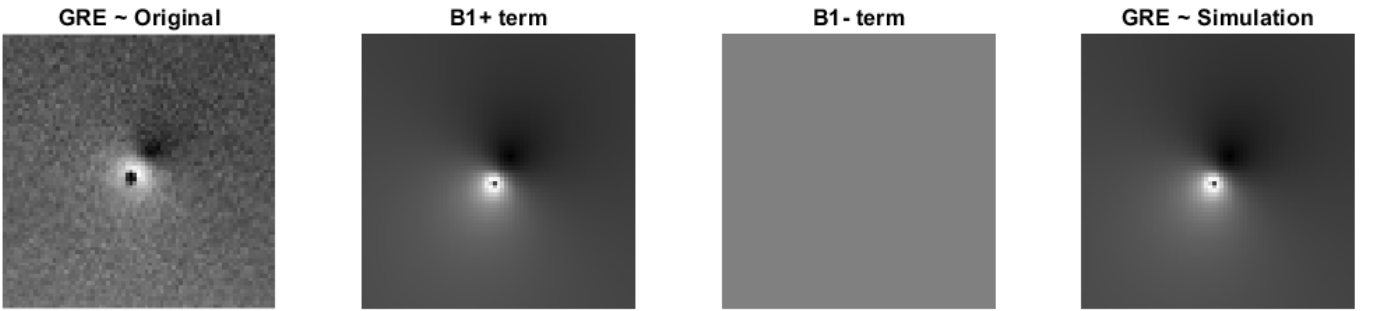


**Figure 3.5:** The original GRE pre-scan image and the separate compartments of the simulation model:  $B_1^+$ ,  $B_1^-$  term, and the final output of the simulation model.

The measured image was fitted to the simulation model using the *fmincon* function of Matlab. This function aimed to minimize the discrepancy between the measured data and the simulation model. It was assumed that the amplitude of the induced current,  $I_{mag}$ , and  $M_0$  are both positive, and that the phase of the induced current,  $I_{phase}$ , ranges between 0 and 360 degrees.

Fitting was done in three different ways:

- The cropped image
- The cropped image with a mask over lead
- The cropped image with a mask over the lead and background



**Figure 3.6:** The three different ways of fitting: cropped GRE pre-scan image, with the addition of a mask over the lead, and a mask over the lead and background.

It was decided to apply a mask over the DBS lead and background of the cropped GRE image since it does not provide any relevant information about the RF coupling, consequently, the induced current to be determined. The mask placement is shown in Figure 3.6.

An example of the fitting procedure is presented in Figure 3.7. The initial guess image and the fitted images using the three different methods were shown. The output variables and the belonging simulation images founded to be slightly different after the fitting procedure. Despite this, the three methods generated images that were comparable to the original image. The three distinct ways for fitting resulted in the production of images that contain significant similarity to one another.

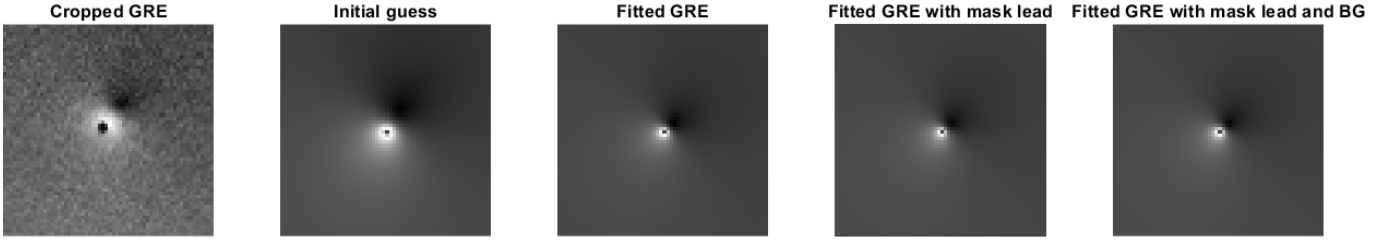


**Figure 3.7:** The original GRE pre-scan image, initial guess and the three fitted methods with corresponding image.

The fitting values of the induced current (magnitude and phase value), and the  $M_0$  were displayed in Table 3.2. In this table it was seen that the fitted values obtained with the addition of masks were the most similar to the initial guess values.

**Table 3.2:** The initial guess and the output values given by the fitting model.

Item	I [mA]	Phase[degree]	$M_0$ [a.u.]
Initial guess	39.4	120	1300
Fitted GRE	18.9	135	1599
Fitted GRE with mask over lead	30.4	140	1570
Fitted GRE with mask over lead and BG	34.0	141	1519

The values for the induced current determined with the semi-automatic approach were used to determine the IF mode. This calculation was done in the same manner as described for the manual approach.

### 3.2.4 Quantitative induced current calculation

In order to enhance the robustness and reliability of the induced current calculation, the aforementioned assumptions are no longer considered valid, and measurements were conducted to determine the actual values of the amplitude of the  $B_{1,inc}^+$  and the nominal flip angle of the incident fields of the two channels of the scanner. The  $B_{1,inc}^+$  amplitude was determined through the use of a TurboFLASH B1map protocol that was available on the scanner. A flip angle map ( $FlipAngle = 80^\circ$ ,  $TR=6830$  msec,  $TE=1.97$  msec, acquisition time = 2 sec,  $FOV= 26\text{cm} \times 26\text{ cm}$ ) was acquired for both calibration scans [41]. This was done by scanning a phantom with the same dimensions as the earlier described phantom, filled solely with the agar-salt mixture. A slice in the center of the phantom was selected, and the average pixel value was calculated to determine the corresponding B1 map values. A pixel value of 800 corresponds to an amplitude value of  $11.74\ \mu\text{T}$ . Based on the measurements and calculations, the  $B_{1,inc}^+$  amplitudes of  $14\ \mu\text{T}$  and  $10\ \mu\text{T}$  were obtained for calibration scans 1 and 2, respectively.

The nominal flip angle of the incident fields of the two channels of the scanner in the case of a human head was expected to be 90 degrees. However, due to non-cylindrical shape of the phantoms used in this study, the phase difference in the center of the phantoms may deviate from the expected value. To address this issue, the previously described phantom was scanned and the central slice was evaluated. Two phase GRE pre-scan images were acquired using the excitation pattern of calibration scan 1 and 2. The pixel values of the phase images were converted to radial values using the scaling factor of  $(-\pi, \pi)$ , which is equivalent to (0,4096). After the conversion, a phase difference map was generated, revealing that the phase difference was measured to be 145 degrees.

# Results

This chapter presents and elucidates the outcomes of the measurements conducted using the previous described phantom. First, the results obtained with the manual approach were explained. Subsequently, the results of the measurements conducted using the model-based approach were described. After this, the outcomes acquired with the advanced induced current calculation were shown.

## 4.1 Manual approach

The manual method was employed to determine safe RF excitation settings, following the procedure outlined in subsection 3.2.2. The outcomes are demonstrated in Figure 4.1, which displays both the whole and cropped GRE images of the calibration scans. The two images on the right contain the point selection, along with the corresponding values for  $r_0$  and  $\phi_0$ . These values were subsequently utilized to determine the induced current and calculate the IF mode. The corresponding IF excitation pattern is presented in Table 4.2 and measured with a low-SAR 2D GRE sequence which is depicted on the left side of Figure 4.6.

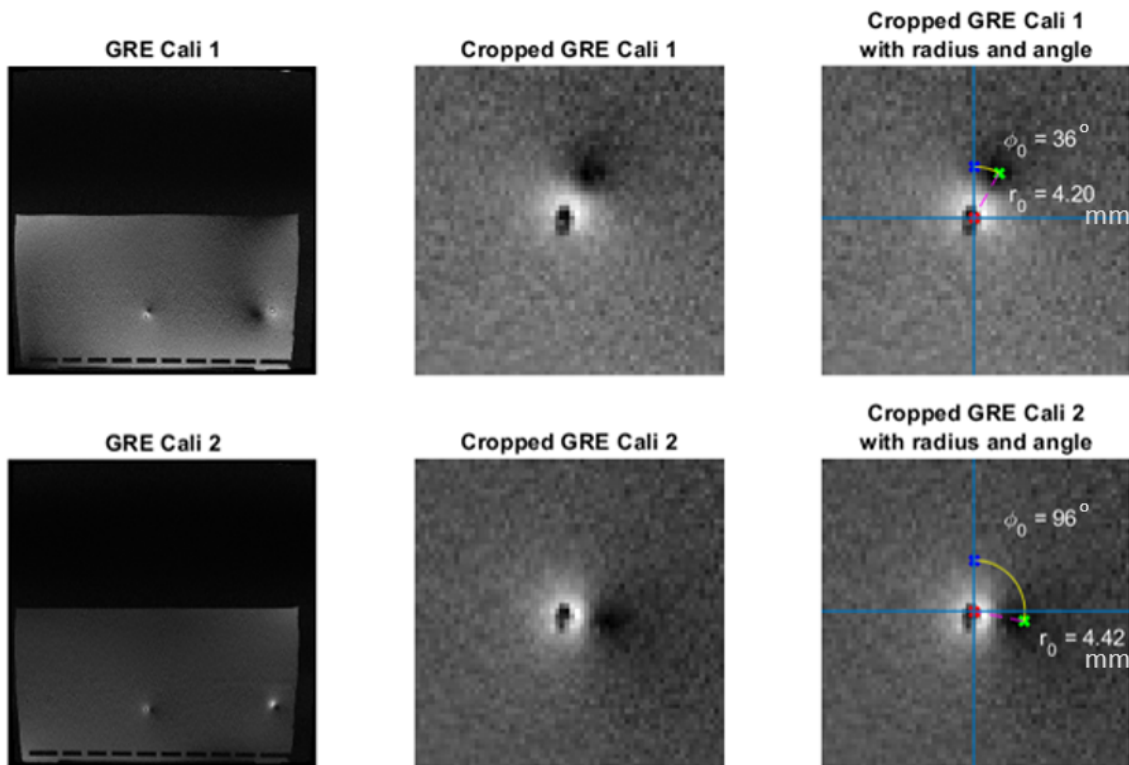


**Figure 4.1:** The whole and cropped GRE images measured with the excitation pattern of calibration scan 1 and 2, and the outcomes obtained from the manual approach.

Whilst executing the manual method, it was noted that accurately and precisely selecting the two points could be challenging. In order to obtain additional insights, the manual approach was executed four times consecutively on identical calibration scans. Figure 4.2a shows the complex values of the induced current, with the values for calibration scan 1 plotted in the top right corner, and calibration scan 2 plotted in the bottom left corner of the figure. The same colour scheme was used for both scans and corresponding IF values were calculated sequentially. These IF values are plotted in Figure 4.2b as a power-phase difference

plot, with the quadrature excitation pattern as the zero point (origin). Inspection of Figure 4.2a revealed that the induced current values for calibration scan 1 were more consistent than those for calibration scan 2. By examining Figure 4.2b, it was observed that all four values are similar. The RF shim values of the four values were within a range of 1.5 dB and had a maximum phase difference of 15 degrees.

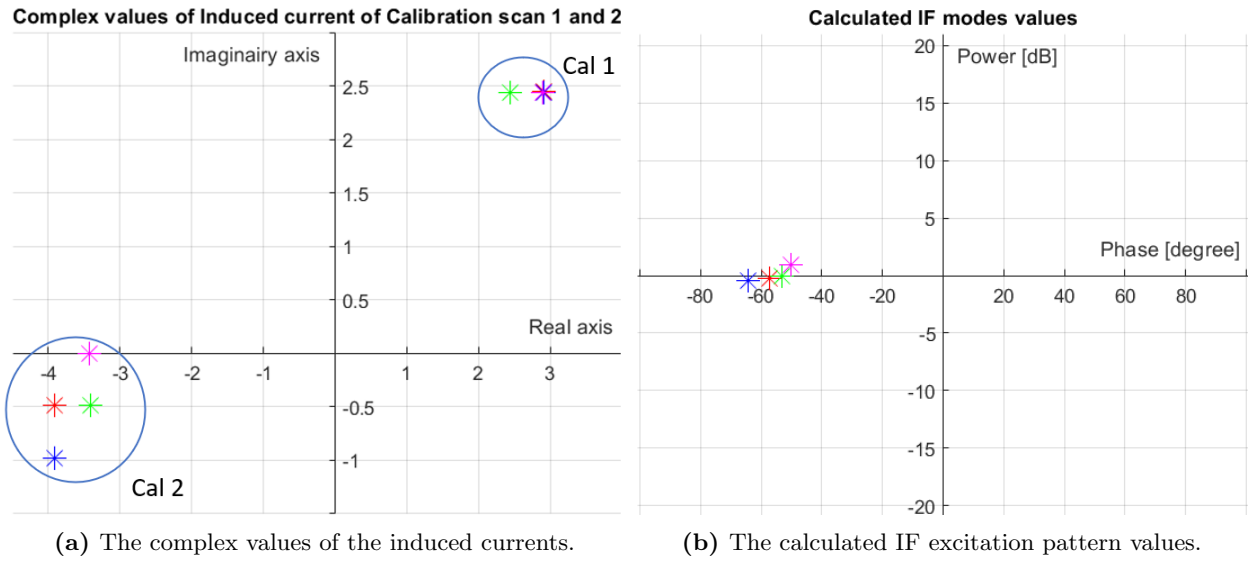


**Figure 4.2:** Multiple determinations of induced current and associated IF mode using the manual method. The colors indicate the corresponding values.

The IF excitation settings were determined and measured utilizing a low-SAR 2D GRE sequence. The resulting images are presented in Figure 4.3. The GRE pre-scans of calibration 1 and 2 are shown on the left, while the remaining four images represent the corresponding IF values as shown in Figure 4.2b. The images of the red, green, and blue point had a higher degree of similarity and were a little closer related to the values in Figure 4.2b. The GRE image measured with the IF mode of the pink point exhibited the least amount of Tx-null artefact, but was not too different from the other three GRE IF mode images.

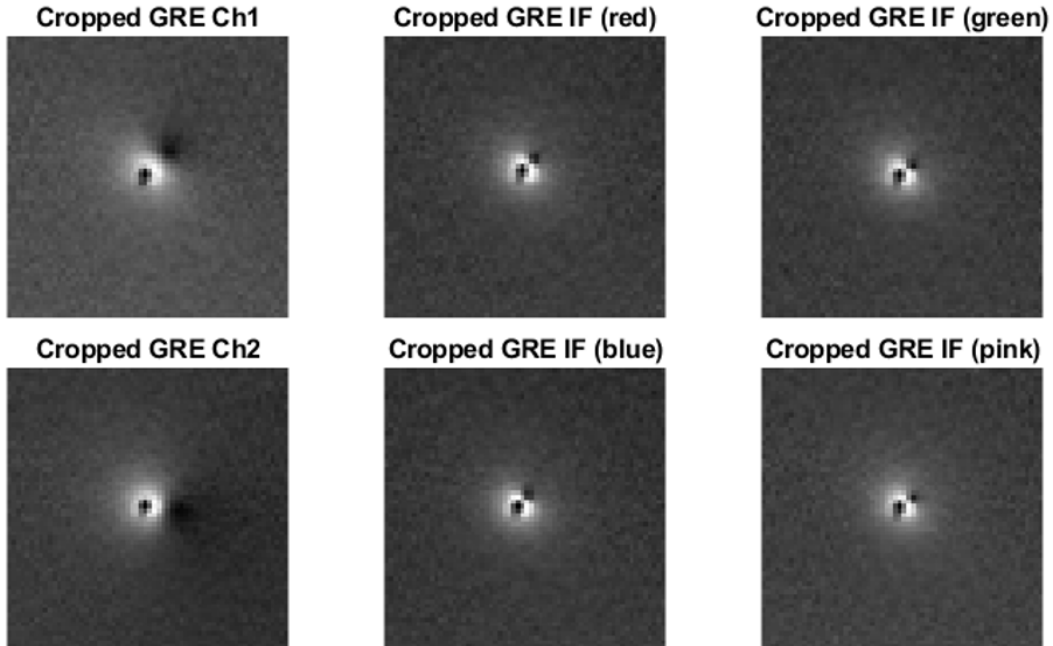


**Figure 4.3:** GRE images measured with the excitation settings of calibration scan 1 and 2, and the four different IF modes indicated by colour.

## 4.2 Model-based approach

In accordance with the methodology detailed in [section 2.2](#), a model-based approach was utilized to determine the IF modes, as described in [subsection 3.2.3](#). The calibration scans displayed in [Figure 4.1](#) were utilized for this purpose. The IF excitation settings were ascertained by employing three different ways, and the resulting simulations were exhibited in [Figures 4.4](#) and [4.5](#), pertaining to calibration scan 1 and 2, respectively.

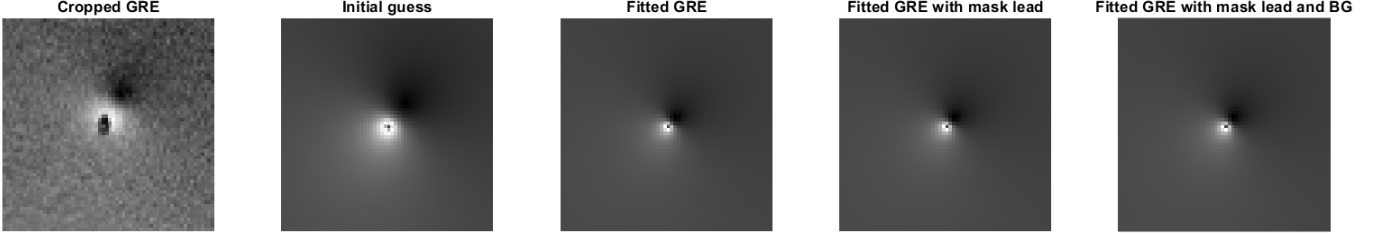


**Figure 4.4:** Results of model-based approach fitting calibration scan 1.

In these figures, it was demonstrated that the employment of a model-based approach results in discernible differences in the corresponding GRE simulations when compared to those generated by the initial guess. Notably, the distinctions between the three fitting methods are not readily apparent through visual analysis. This effect was observed consistently across both calibration scans.

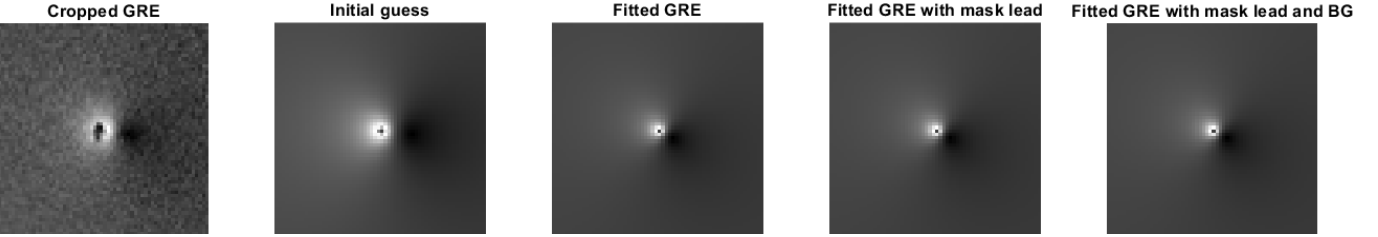


**Figure 4.5:** Results of model-based approach fitting calibration scan 2.

The fitting values of the induced current (magnitude and phase value), the  $M_0$ , and the cost value are displayed in [Table 4.1](#). The cost value presents the difference between the measured and simulated GRE matrix and indicated that the incorporation of masks gave fitted values that contained greater concordance with the initial guess values. Moreover, the model-based approach that included the mask over the deep brain stimulation (DBS) lead and background demonstrated the lowest cost value. Therefore, this fitting approach was selected for comparative analysis between the various methods. The calculated IF mode of the three approaches are displayed in [Table 4.2](#) and the corresponding GRE images are shown in [Figure 4.6](#).

**Table 4.1:** The initial guess and the output values given by the semi-automatic model for calibration scan 1 and 2.

Cal scan	Fitting approach	I [mA]	Phase [degree]	$M_0$ [a.u.]	Cost value [a.u.]
1	Initial guess	42.0	36	1300	4668
	Without mask	17.0	40	1523	3159
	With mask over lead	31.8	49	1477	3018
	With mask over lead and BG	35.9	49	1412	2920
2	Initial guess	44.2	186	1300	3777
	Without mask	21.2	210	1339	2463
	With mask over lead	28.6	196	1378	1742
	With mask over lead and BG	30.5	195	1374	1590

### 4.3 Quantitative induced current calculation

The impact of incorporating the  $B_{1,inc}^+$  field amplitude and phase difference between the two transmit channels was assessed using the same calibration scans shown in Figure 4.1. The resulting values of the IF modes are presented in Table 4.2. Figure 4.6 displays the IF mode obtained from the inclusion of the  $B_{1,inc}^+$  amplitude, whereas no visualization of the incorporation of both the  $B_{1,inc}^+$  amplitude and phase difference was available due to a calculation error during the measurement.

### 4.4 Assessment of methods

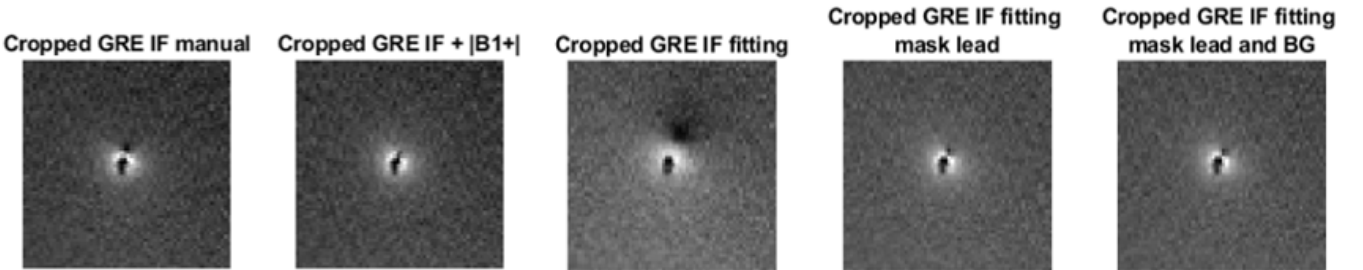
An assessment had been made between the results obtained during the T2\_TSE measurement performed with the IF outcomes of the three previously described methods. The resulting IF excitation settings are displayed in Table 4.2.

**Table 4.2:** The magnitude and phase values for Ch1 and Ch2 for different excitation pattern.

Excitation pattern	Ch1	Ch2
Manual approach	0.73 $\angle 0^\circ$	0.69 $\angle 29^\circ$
Model-based approach without mask	0.99 $\angle 0^\circ$	0.17 $\angle 10^\circ$
Model-based approach with mask over lead	0.67 $\angle 0^\circ$	0.74 $\angle 33^\circ$
Model-based approach with mask over lead and BG	0.65 $\angle 0^\circ$	0.76 $\angle 35^\circ$
Addition of $B_{1,inc}^+$ amplitude	0.61 $\angle 0^\circ$	0.80 $\angle 27^\circ$
Addition of $B_{1,inc}^+$ amplitude and phase difference transmit channels *	0.61 $\angle 0^\circ$	0.80 $\angle 293^\circ$

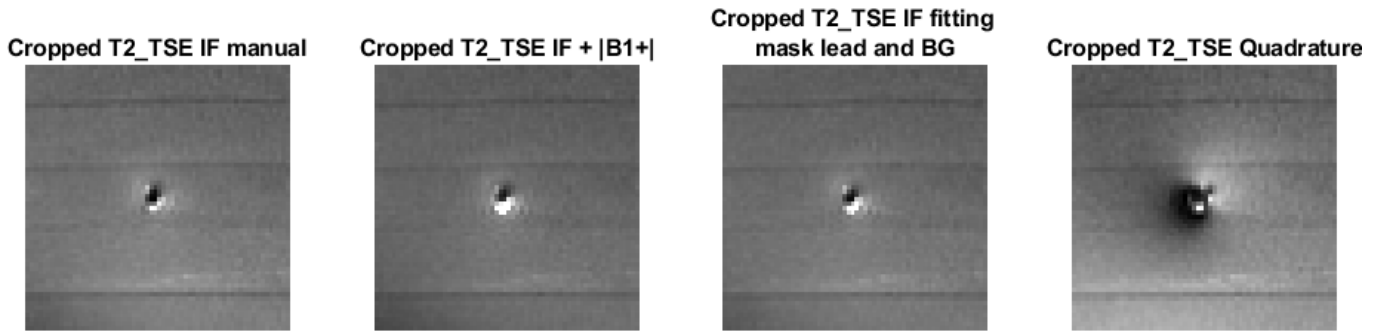
\*This value was obtained after the measurement, as a calculation error had arose during the measurement process.

Figure 4.6 displays the GRE pre-scans of the different IF mode outcomes. It was apparent that the IF mode of the manual method and the model-based approach with a mask over DBS lead and mask over DBS lead and background had resulted in quite similar images in terms of the size and location of the Tx-null. Although the Tx-null was less prominent than in the calibration scans, it had not completely vanished. However, the addition of the  $B_{1,inc}^+$  amplitude for calculating the IF mode had a positive impact on eliminating the Tx-null.



**Figure 4.6:** The IF modes determined with the manual approach, model-based approach and the addition of  $B_{1,inc}^+$  amplitude.

The effectiveness and safety of the proposed methods was evaluated by quantifying the temperature rise near the tip of the DBS lead and assessing the visual image quality for both the safe RF excitation pattern determined with the manual approach, model-based approach with mask over DBS lead and BG, and with the addition of the  $B_{1,inc}^+$  amplitude. Figure 4.7 presents images captured 1 cm above the tip. Upon visual comparison, it was observed that the use of an IF mode results in higher image quality as compared to quadrature settings. The latter exhibited an artefact adjacent to the DBS lead, which could cause difficulties in placement evaluation. Upon comparing the three IF mode images, slight differences were observable. The  $B_{1,inc}^+$  amplitude and model-based approach using a mask over the DBS lead and background exhibited a relatively more prominent white border around the lead as compared to the manual method.



**Figure 4.7:** The T2\_TSE image of the three different IF mode outcomes and the quadrature setting, obtained 1 cm above the tip.

The real-time temperature rise at the tip of the DBS lead measured during a T2\_TSE protocol are plotted in Figure 4.8. It was observed that there exists a noticeable distinction between the reference measurement (quadrature) and the three IF modes, wherein the latter exhibit a substantially lower temperature increase. The temperature measurements obtained using the manual method and fittings model were found to be comparable. The inclusion of  $B_{1,inc}^+$  amplitude provided the least temperature increase.

The temperature rise of the background (plotted in green) was also recorded and plotted in Figure 4.8. In this figure the background temperature measurement recorded with the manual IF excitation pattern was plotted. Analysis of the background measurements showed that the maximum temperature increase in the background remained constant regardless of the excitation pattern applied, see Appendix D Figure D.1. In Figure 4.8, it is seen that the IF modes attained a heating level that is comparable to the level obtained by the background measurement.

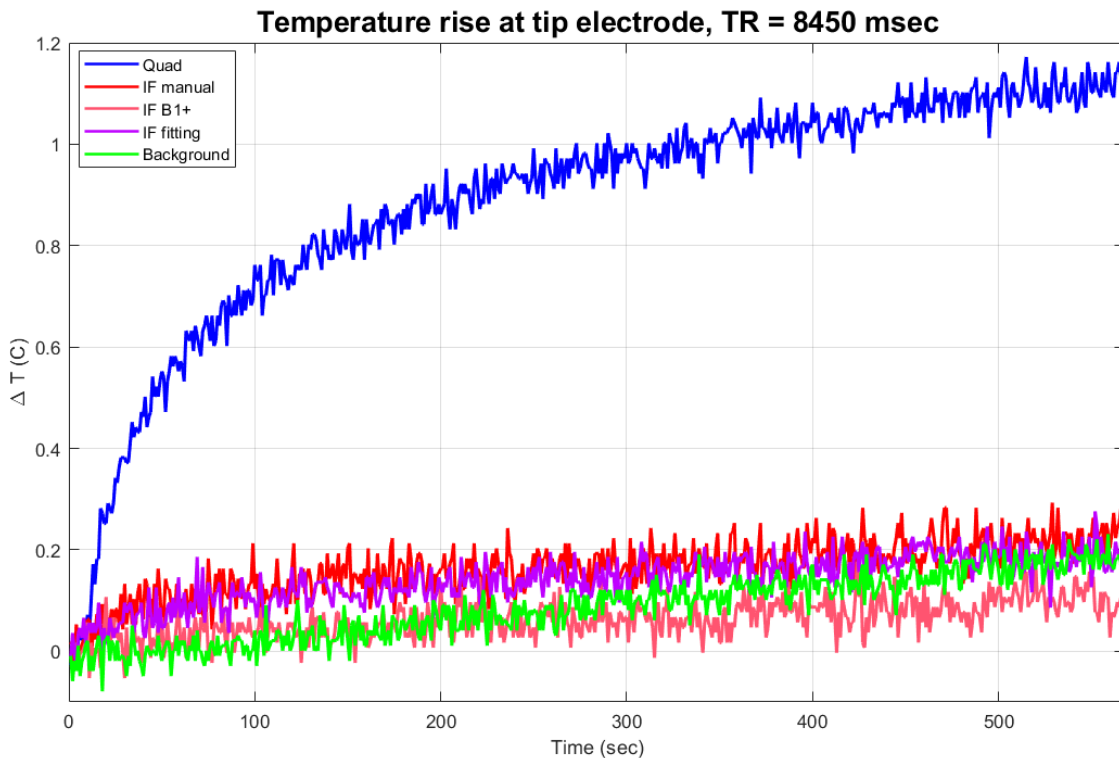


**Figure 4.8:** Four different excitation patterns were employed during the T2\_TSE sequence measurements.

The predicted safety values obtained from the temperature measurements are presented in Table 4.3, indicating that the measurements were performed at a similar RF power, which permits a valid comparison. Furthermore, the predicted values for both whole-body SAR and  $B_{1,rms}^+$  were consistent across all four measurements.

**Table 4.3:** The predicted safety values of the measured RF shim settings.

<b>Temperature measurement</b>	<b>SAR whole body (%)</b>	<b>SAR head local (%)</b>	<b><math>B_{1,rms}^+</math> (<math>\mu</math>T)</b>	<b>RF power (W)</b>
Manual approach	37.5	99.1	1.53	19.29
Model-based approach with mask over lead and BG	35.6	83.3	1.49	18.75
Addition of $B_{1,inc}^+$ amplitude	35.1	83.6	1.49	18.67
Quadrature	35.7	63.4	1.50	18.70

# Discussion

This chapter presents the discussion of the obtained results, followed by the limitations of this study and suggestions for future research.

## 5.1 Discussion

There is a desire from the clinic that calls for a patient-specific method that can be safely used to scan patients with an implanted DBS system at 3T MRI [1]. In this study, we have evaluated the feasibility of a patient-specific method which works on a manually manner. In order to facilitate the integration of this method into clinical practice, it is imperative to mitigate the user dependency associated with the manual approach. To address this, a model-based approach has been developed, incorporating the fundamental principles of the manual method, with the aim of alleviating the user dependency. A single measurement setup is utilized to compare and evaluate the performance of manual and semi-automatic method.

In this setup, it is feasible to mitigate the effects of induced current and Tx-null artefact around the DBS lead by implementing the manual method when utilizing the IF mode. Furthermore, the obtained temperature measurement indicates a lower degree of heating when employing the IF excitation pattern, in contrast to the quadrature setting. Nevertheless, it is imperative to acknowledge that the manual approach is not without limitations.

One such limitation pertains to the precision from which the location of the two points, i.e. the lead and Tx-null, are selected. The accuracy of this process is heavily reliant on the observer's level of training, with a well-trained individual being better equipped to discern variations in intensity and facilitate the selection of the darkest pixel for both points. Furthermore, the selection of the points is also dependent on the resolution and location of the Tx-null. All of these factors can result in an inaccurate selection of points, which can potentially result in miscalculations of induced current and, consequently, the excitation pattern of the IF mode. The impact of multiple selections of the two points by the same experienced observer is investigated. Analysis of the outcomes indicate that the calculated induced currents fall within the same complex value region. Similar observations are noted with regards to the IF mode outcomes, where a difference of 1.5 dB and 15 degrees is observed. Notably, the corresponding images do not demonstrate significant disparities in Tx-null location and size.

Inclusion of the  $B_{1,inc}^+$  amplitude in the induced current calculation is an essential step in this method. This adjustment leads to a further reduction in RF heating and yields a visual improvement in image quality. Conversely, the addition of the phase difference between the two transmit channels of the scanner has not demonstrated such effects, contrary to initial expectations. Further research is required to draw a more definitive conclusion regarding the impact of this addition.

To facilitate the integration of the off-label method in clinical practice, it is crucial to address the issues of inaccuracy and user-dependence in the manual approach. A model-based approach that utilizes a simulation model that replicates the signal intensity of a GRE image, can potentially serve as a solution. The model-based approach involves the determination of a set of parameters that minimize the difference between the measured and simulated GRE image. Three different approaches are evaluated and the results indicate that incorporating a mask is necessary to produce a more reliable IF mode. So, the model-based approach is capable of generating a comparable but more robust and safer outcome for the mitigation of RF field enhancement. Thereby, it provides a future perspective for the integration of this method in clinical setting. Furthermore, the additional scans required for the proposed method, including GRE pre-scans

and TurboFlash B1map, are of short duration and can be easily integrated into clinical practise without imposing any significant limitations.

The current assessment of image quality relies solely on visual inspection, which is not sufficient to draw quantitative conclusions. One approach is to measure the average signal intensity around the lead and across the entire image in both the IF and quadrature mode [1]. Additionally, a neurosurgeon's evaluation of the image quality around the lead position could be utilized as qualitative method.

It has been established that the localizer and low-SAR 2D GRE sequence are safe for usage. The safety values, which are expressed in SAR and  $B_{1,rms}^+$ , are sufficiently low to permit their application in a scenario where a single lead is implanted. The sequences have a short duration, which prevents a significant increase in scan time. Nevertheless, there is a pronounced necessity to modify the sequence employed for determining slice position in a low SAR protocol. This can be accomplished by reducing the flip angle [42]. Upon modifying the experimental setup, it is imperative to conduct a thorough re-evaluation of all sequences encompassed within the scanning protocol.

During temperature measurements, safety values expressed in SAR and  $B_{1,rms}^+$  are predicted by the scanner. The IF excitation patterns are expected to result in higher local heating at the tip, as they have a local head SAR higher than 80%, in comparison with quadrature settings (local head SAR of around 60%). Real-time temperature measurements around the tip show that the heating is significantly lower for the IF modes than for quadrature. Additionally, it can be inferred that the local antenna effect around the tip of the DBS lead is no longer prevalent since the IF modes and background temperature measurements produce equivalent levels of heating.

At this moment, it is unknown how the manufacturer of the scanner calculates the predicted safety values. To integrate the proposed method into clinical practice, it is necessary to establish safety standards for scanning DBS patients. In future research, the importance of SAR values in the determination of patient safety, and whether  $B_{1,rms}^+$  can provide sufficient indication of safety is required.

The duration of the temperature measurements conducted in this study correspond to the sequences commonly employed in clinical settings. Considering that this method is deemed safe, regardless of the approach used, it is reasonable to assert that the resulting tip heating in cases where a single DBS lead is implanted would comply with the established safety heating standards. This offers a promising outlook for the safe integration of this method into clinical practice.

## 5.2 Limitations

The phase difference between the transmit channels is determined using a different phantom than the one used during the measurement. Although the dimensions are the same, it is assumed that the position of the slice for phase determination of the two transmit channels is the same as that in the phantom used for the measurements. Nonetheless, it is important to consider that there may be some variation due to this difference. In future studies, this issue can be addressed by measuring a slice under the tip. This approach can also be used for determining the  $B_{1,inc}^+$  amplitude.

The Matlab script utilized for the selection of two positions in the GRE images (manual approach) is reliant on the selected pixel. Although the script has been programmed to select the nearest pixel as the location, this method may lead to erroneous pixel selection, which can affect subsequent calculations. This could have an impact on the value of the induced current and, consequently, on the IF mode. Nonetheless, the influence is anticipated to be insignificant, given the small size of the pixels.

The current model-based approach employs the manual method to determine the initial guess. However, in order to utilize this off-label method in clinical practice, an fully automated approach is desired. This will eliminate user dependency and offers the advantage of reducing the time required to perform the method. Although this has been attempted during this study, it has not yet been achieved. Future research is recommended to further explore this issue.

In this study, the DBS lead is positioned straight into the phantom, but it is important to note that the lead in the phantom may not be exactly straight aligned parallel to  $B_0$  field. The GRE image is selected perpendicular to the tip of the lead, and any small angle deviation could potentially affect the determination of the induced current and IF mode. However, the effect of this deviation is expected to be negligible for the situations examined in this study.

The current study uses a temperature probe attached only at the tip, neglecting other locations along the lead. Nevertheless, it is established that the induced current flows throughout the entire length of the lead. Variations in electrical properties of different tissue types (brain, muscle, and fat) affect the local electrical field around the lead [6]. To provide comprehensive safety evaluation surrounding the complete lead, the placement of the temperature probe at other points can be considered.

The agar mix utilized in this study is capable of emulating the electrical properties of brain tissue. Nevertheless, biological structures including white and gray matter variations and blood vessels are not accounted for. According to several studies, perfusion has a mitigating effect on the temperature surrounding the lead [43, 44]. This implies that the in-vivo condition is potentially safer than the current measured scenario.

### 5.3 Future recommendations

The model-based approach presents an opportunity for safe scanning of patients with implanted DBS systems in clinical applications with a 3T MRI scanner. However, before this method can be integrated into the clinic, certain modifications are required. For instance, the size of the mask across the tip can be varied to optimize the model-based approach. Furthermore, a lower-resolution GRE pre-scan can be considered, as this would yield higher signal-to-noise ratios and possibly facilitate a more accurate fitting of the simulation model, resulting in a lower cost value. Another area for investigation is the assumption that the  $B_1^-$  field is not homogeneous, and the evaluation of lower and upper bound settings. Next to this, the incorporation of the  $B_{1,inc}$  field amplitude can be included within the quasi-static RF field model. By further optimizing the model-based approach, progress can be made toward developing an automated model. An automated model would need to be achieved before this method can be used in the clinic to remove the remaining user-dependency and reduce the procedure time.

In a clinical setting, DBS leads are typically not inserted straight into the brain, but rather placed in an oblique orientation. This study did not evaluate the method in situations where the lead was angled. Further investigation could be carried out to test the feasibility of the method in such situations. In cases where the lead is oblique, a 3D GRE recording can be necessary to calculate the angular rotation. Nevertheless, performing a multi-slice recording may result in a safety problem due to the higher power required during scanning. The heating observed at the tip could be greater in a multi-slice situation and would require further investigation.

In typical DBS procedures, the placement of two leads in the target regions is common. To enable the translation of this method in clinical practice, the implications of this situation must be carefully assessed. It is anticipated that the induced current cannot be completely eliminated, but rather that a minimal level of current must be targeted. If the minimal scenario is deemed unsafe for the patient, the use of multiple transmission channels could be considered. Simulation models and experiments have been employed in several studies to explore the feasibility of this application [45, 46, 47].

To enhance the comprehension of heating effects surrounding the DBS lead, a subsequent investigation could explore the creation of an EM/thermal simulation model [30]. The simulation model can forecast the level of heating for various geometry configurations of the DBS system by using the derived transimpedance value, hence, minimizing the necessity for numerous phantom setups and real-time temperature measurements. Through an EM/thermal simulation model, additional knowledge can be acquired regarding the impact of different geometries (i.e. placement and length of leads) of the DBS system without actual setup execution. Additionally, such a simulation model could explore diverse field strengths and scenarios where the tip of the lead is positioned off-center in the bore.

## 5.4 Future perspectives

In order to assess the universality of this method, further investigation involving testing with different types and brands of DBS leads will be necessary. Such testing can involve evaluating leads manufactured by Abbott or Medtronic and assessing the performance of standard lead configurations as opposed to directional ones. Moreover, it is imperative to conduct testing with different types of scanners, receiver coils, and field strengths to ensure the generalizability of the proposed method.

During initial measurements, it is found that the location of the Tx-null artefact is sometimes challenging to visualize due to its close proximity to the lead or its small size. Thus, it is recommended to utilize multiple calibration scans in such instances to accurately determine the IF mode.

The initial measurements carried out with the described setup involved an IPG that was embedded in agar. The obtained results revealed pre-scans in which the Tx-null artefact exhibited minimal positional changes, rendering it challenging to deduce the induced currents and subsequently the IF mode. This was because the distance between the IPG and the tip of the DBS lead was too close, leading to most of the RF heating dissipated to the surrounding agar at the IPG. For future studies, the IPG can be given less consideration since the distance between the lead and IPG is greater in a clinical setting, and there is more adipose tissue surrounding the IPG, thus reducing the risk of excessive temperature rise.

# Conclusion

The study findings indicate that the Tx-null artefact can be utilized in low-SAR 2D GRE pre-scans for determining RF excitation parameters that are within the safety threshold for brain tissue heating. Additionally, the image quality visibly improved compared to the conventional quadrature settings. This study also aimed to gain insight into the phenomenon of RF field enhancement. This was accomplished through the development of a quasi-static RF field model. Our temperature measurements on both phantoms showed that the IF mode led to a reduction in RF heating at the tip of the lead in all cases compared to the quadrature settings. We also explored two approaches to calculate the induced current and IF mode. The applicability of the manual approach in determining an IF mode has been demonstrated through the utilization of GRE calibration scans. Drawing upon these established principles, a model-based approach has been devised to further advance the methodology. Our model-based approach holds promise for potential integration into the clinic, as it provides a more robust and reliable solution while removing user dependency.

In conclusion, this study provides valuable insights and methods for predicting induced currents, determining safe RF excitation settings, and visually improving image quality in DBS procedures. The developed quasi-static RF field model within the semi-automatic based approach offer potential solutions for reducing RF coupling and improving safety in DBS procedures, and further investigation is warranted to evaluate its potential for clinical implementation.



# Bibliography

- [1] Y. Eryaman, N. Kobayashi, S. Moen, J. Aman, A. Grant, J. T. Vaughan, G. Molnar, M. C. Park, J. Vitek, G. Adriany, K. Ugurbil, and N. Harel, “A simple geometric analysis method for measuring and mitigating RF induced currents on Deep Brain Stimulation leads by multichannel transmission/reception,” *NeuroImage*, vol. 184, pp. 658–668, jan 2019.
- [2] W. Poewe, K. Seppi, C. M. Tanner, G. M. Halliday, P. Brundin, J. Volkman, A. E. Schrag, and A. E. Lang, “Parkinson disease,” *Nature Reviews Disease Primers*, vol. 3, pp. 1–21, mar 2017.
- [3] C. E. McElcheran, B. Yang, K. J. Anderson, L. Golestanirad, and S. J. Graham, “Parallel radiofrequency transmission at 3 tesla to improve safety in bilateral implanted wires in a heterogeneous model,” *Magnetic Resonance in Medicine*, vol. 78, no. 6, pp. 2406–2415, 2017.
- [4] J. Nicole Bentley, Z. Guan, K. S. Cummings, K. L. Chou, and P. G. Patil, “Influence of Intracranial Air on Electrode Position and Clinical Outcomes following Deep Brain Stimulation for Parkinson’s Disease,” *Stereotactic and Functional Neurosurgery*, vol. 95, no. 1, pp. 6–12, 2017.
- [5] I. Barnaure, P. Pollak, S. Momjian, J. Horvath, K. O. Lovblad, C. Boëx, J. Remuinan, P. Burkhard, and M. I. Vargas, “Evaluation of electrode position in deep brain stimulation by image fusion (MRI and CT),” *Neuroradiology*, vol. 57, no. 9, pp. 903–908, 2015.
- [6] B. Bhusal, B. T. Nguyen, P. P. Sanpitak, J. Vu, B. Elahi, J. Rosenow, M. J. Nolt, R. Lopez-Rosado, J. Pilitsis, M. Dimarzio, and L. Golestanirad, “Effect of Device Configuration and Patient’s Body Composition on the RF Heating and Nonsusceptibility Artifact of Deep Brain Stimulation Implants During MRI at 1.5T and 3T,” 2020.
- [7] J. Spiegel, G. Fuss, M. Backens, W. Reith, T. Magnus, G. Becker, J. R. Moringlane, and U. Dillmann, “Transient dystonia following magnetic resonance imaging in a patient with deep brain stimulation electrodes for the treatment of Parkinson disease: Case report,” *Journal of Neurosurgery*, vol. 99, pp. 772–774, oct 2003.
- [8] L. Zrinzo, F. Yoshida, M. I. Hariz, J. Thornton, T. Foltynie, T. A. Yousry, and P. Limousin, “Clinical safety of brain magnetic resonance imaging with implanted deep brain stimulation hardware: Large case series and review of the literature,” jul 2011.
- [9] J. M. Henderson, J. Thach, M. Phillips, K. Baker, F. G. Shellock, and A. R. Rezai, “Permanent neurological deficit related to magnetic resonance imaging in a patient with implanted deep brain stimulation electrodes for Parkinson’s disease: Case report,” *Neurosurgery*, vol. 57, p. 1063, nov 2005.
- [10] M. R. Van Den Bosch, M. A. Moerland, J. J. W. Lagendijk, L. W. Bartels, and C. A. T. Van Den Berg, “New method to monitor RF safety in MRI-guided interventions based on RF induced image artefacts,” 2010.
- [11] A. Boutet, R. Gramer, C. J. Steele, G. J. Elias, J. Germann, R. Maciel, W. Kucharczyk, L. Zrinzo, A. M. Lozano, and A. Fasano, “Neuroimaging Technological Advancements for Targeting in Functional Neurosurgery,” jul 2019.
- [12] K. B. Baker, J. Tkach, J. D. Hall, J. A. Nyenhuis, F. G. Shellock, and A. R. Rezai, “Reduction of magnetic resonance imaging-related heating in deep brain stimulation leads using a lead management device,” *Neurosurgery*, vol. 57, oct 2005.

- [13] W. Kainz, G. Neubauer, R. Überbacher, F. Alesch, and D. D. Chan, "Temperature measurement on neurological pulse generators during MR scans," *BioMedical Engineering Online*, vol. 1, pp. 1–8, sep 2002.
- [14] R. W. Gray, W. T. Bibens, and F. G. Shellock, "Simple design changes to wires to substantially reduce MRI-induced heating at 1.5 T: Implications for implanted leads," *Magnetic Resonance Imaging*, vol. 23, pp. 887–891, oct 2005.
- [15] P. A. Bottomley, A. Kumar, W. A. Edelstein, J. M. Allen, and P. V. Karmarkar, "Designing passive MRI-safe implantable conducting leads with electrodes," *Medical Physics*, vol. 37, no. 7, pp. 3828–3843, 2010.
- [16] M. M. Elwassif, A. Datta, A. Rahman, and M. Bikson, "Temperature control at DBS electrodes using a heat sink: Experimentally validated FEM model of DBS lead architecture," *Journal of Neural Engineering*, vol. 9, no. 4, 2012.
- [17] P. Serano, L. M. Angelone, H. Katnani, E. Eskandar, and G. Bonmassar, "A novel brain stimulation technology provides compatibility with MRI," *Scientific Reports*, vol. 5, 2015.
- [18] T. Herrington, L. M. Angelone, L. L. Wald, E. Adalsteinsson, C. LaPierre, A. Mareyam, and L. L. Wald, "Construction and modeling of a reconfigurable MRI coil for lowering SAR in patients with deep brain stimulation implants," *NeuroImage*, vol. 147, pp. 577–588, feb 2017.
- [19] Y. Eryaman, E. A. Turk, C. Oto, O. Algin, and E. Atalar, "Reduction of the radiofrequency heating of metallic devices using a dual-drive birdcage coil," *Magnetic Resonance in Medicine*, vol. 69, pp. 845–852, mar 2013.
- [20] D. Shrivastava, A. Abosch, J. Hughes, U. Goerke, L. Delabarre, R. Visaria, N. Harel, and J. Thomas Vaughan, "Heating induced near deep brain stimulation lead electrodes during magnetic resonance imaging with a 3 T transceive volume head coil," *Physics in Medicine and Biology*, vol. 57, no. 17, pp. 5651–5665, 2012.
- [21] L. Golestanirad, L. M. Angelone, M. I. Iacono, H. Katnani, L. L. Wald, and G. Bonmassar, "Local SAR near deep brain stimulation (DBS) electrodes at 64 and 127 MHz: A simulation study of the effect of extracranial loops," *Magnetic Resonance in Medicine*, vol. 78, no. 4, pp. 1558–1565, 2017.
- [22] Y. Eryaman, B. Akin, and E. Atalar, "Reduction of implant RF heating through modification of transmit coil electric field," *Magnetic Resonance in Medicine*, vol. 65, no. 5, pp. 1305–1313, 2011.
- [23] M. A. Bernstein, J. Huston, and H. A. Ward, "Imaging artifacts at 3.0T," oct 2006.
- [24] Y. Eryaman, B. Guerin, C. Akgun, J. L. Herraiz, A. Martin, A. Torrado-Carvajal, N. Malpica, J. A. Hernandez-Tamames, E. Schiavi, E. Adalsteinsson, and L. L. Wald, "Parallel transmit pulse design for patients with deep brain stimulation implants," *Magnetic Resonance in Medicine*, vol. 73, no. 5, pp. 1896–1903, 2015.
- [25] C. E. McElcheran, B. Yang, K. J. Anderson, L. Golestanirad, and S. J. Graham, "Investigation of parallel radiofrequency transmission for the reduction of heating in long conductive leads in 3 Tesla magnetic resonance imaging," *PLoS ONE*, vol. 10, no. 8, p. 134379, 2015.
- [26] L. Golestanirad, B. Keil, L. M. Angelone, G. Bonmassar, A. Mareyam, and L. L. Wald, "Feasibility of using linearly polarized rotating birdcage transmitters and close-fitting receive arrays in MRI to reduce SAR in the vicinity of deep brain simulation implants," *Magnetic Resonance in Medicine*, vol. 77, pp. 1701–1712, apr 2017.
- [27] M. V. Vaidya, C. M. Collins, D. K. Sodickson, R. Brown, G. C. Wiggins, and R. Lattanzi, "Dependence of B1- and B1+ field patterns of surface coils on the electrical properties of the sample and the MR operating frequency," *Concepts in Magnetic Resonance Part B: Magnetic Resonance Engineering*, vol. 46, pp. 25–40, feb 2016.

- [28] A. A. Gupte, D. Shrivastava, M. A. Spaniol, and A. Abosch, "MRI-related heating near deep brain stimulation electrodes: More data are needed," jun 2011.
- [29] M. I. Iacono, N. Makris, L. Mainardi, L. M. Angelone, and G. Bonmassar, "MRI-based multiscale model for electromagnetic analysis in the human head with implanted DBS," *Computational and Mathematical Methods in Medicine*, vol. 2013, 2013.
- [30] A. Sadeghi-Tarakameh, N. I. H. Zulkarnain, X. He, E. Atalar, N. Harel, and Y. Eryaman, "A workflow for predicting temperature increase at the electrical contacts of deep brain stimulation electrodes undergoing MRI," *Magnetic Resonance in Medicine*, vol. 88, pp. 2311–2325, nov 2022.
- [31] J. P. Tokaya, A. J. Raaijmakers, P. R. Luijten, J. F. Bakker, and C. A. van den Berg, "MRI-based transfer function determination for the assessment of implant safety," *Magnetic Resonance in Medicine*, vol. 78, pp. 2449–2459, dec 2017.
- [32] D. I. Hoult, "The principle of reciprocity in signal strength calculations - A mathematical guide," *Concepts in Magnetic Resonance*, vol. 12, no. 4, pp. 173–187, 2000.
- [33] G. Fierens, N. Standaert, R. Peeters, C. Glorieux, and N. Verhaert, "Safety of active auditory implants in magnetic resonance imaging," jul 2021.
- [34] A. Boutet, G. J. Elias, R. Gramer, C. Neudorfer, J. Germann, A. Naheed, N. Bennett, B. Li, D. Gwun, C. T. Chow, R. Maciel, A. Valencia, A. Fasano, R. P. Munhoz, W. Foltz, D. Mikulis, I. Hancu, S. K. Kalia, M. Hodaie, W. Kucharczyk, and A. M. Lozano, "Safety assessment of spine MRI in deep brain stimulation patients," *Journal of Neurosurgery: Spine*, vol. 32, pp. 973–983, feb 2020.
- [35] J. Kahan, A. Papadaki, M. White, L. Mancini, T. Yousry, L. Zrinzo, P. Limousin, M. Hariz, T. Foltynie, and J. Thornton, "The safety of using body-transmit MRI in patients with implanted deep brain stimulation devices," *PLoS ONE*, vol. 10, no. 6, 2015.
- [36] F. Sammartino, V. Krishna, T. Sankar, J. Fisico, S. K. Kalia, M. Hodaie, W. Kucharczyk, D. J. Mikulis, A. Crawley, and A. M. Lozano, "3-Tesla MRI in patients with fully implanted deep brain stimulation devices: A preliminary study in 10 patients," *Journal of Neurosurgery*, vol. 127, no. 4, pp. 892–898, 2017.
- [37] D. A. Finelli, A. R. Rezai, P. M. Ruggieri, J. A. Tkach, J. A. Nyenhuis, G. Hrdlicka, A. Sharan, J. Gonzalez-Martinez, P. H. Stypulkowski, and F. G. Shellock, "MR Imaging-Related Heating of Deep Brain Stimulation Electrodes: In Vitro Study," *AJNR: American Journal of Neuroradiology*, vol. 23, p. 1795, nov 2002.
- [38] Boston Scientific, "Vercise DBS Leads: Directions for Use," *Accessed at <https://www.bostonscientific.com/content/dam/Manuals/us>*, 2018.
- [39] Boston Scientific Corporation., "Vercise™ DBS system. Boston Scientific Corporation.."
- [40] "TempSens signal conditioner for temperature measurement."
- [41] S. Chung, D. Kim, E. Breton, and L. Axel, "Rapid B1+ mapping using a preconditioning RF pulse with turboFLASH readout," *Magnetic Resonance in Medicine*, vol. 64, no. 2, pp. 439–446, 2010.
- [42] A. Boutet, I. Hancu, U. Saha, A. Crawley, D. S. Xu, M. Ranjan, E. Hlasny, R. Chen, W. Foltz, F. Sammartino, A. Coblenz, W. Kucharczyk, and A. M. Lozano, "3-Tesla MRI of deep brain stimulation patients: safety assessment of coils and pulse sequences," *Journal of Neurosurgery*, vol. 132, pp. 586–594, feb 2019.
- [43] M. Salcman, E. Moriyama, H. J. Elsner, H. Rossman, R. A. Gettleman, G. Neuberth, and G. Corradino, "Cerebral blood flow and the thermal properties of the brain: A preliminary analysis," *Journal of Neurosurgery*, vol. 70, pp. 592–598, apr 1989.

- 
- [44] C. M. Collins, M. B. Smith, and R. Turner, “Model of local temperature changes in brain upon functional activation,” *Journal of Applied Physiology*, vol. 97, pp. 2051–2055, dec 2004.
- [45] M. Etezadi-Amoli, P. Stang, A. Kerr, J. Pauly, and G. Scott, “Controlling radiofrequency-induced currents in guidewires using parallel transmit,” *Magnetic Resonance in Medicine*, vol. 74, pp. 1790–1802, dec 2015.
- [46] B. Guerin, L. M. Angelone, D. Dougherty, and L. L. Wald, “Parallel transmission to reduce absorbed power around deep brain stimulation devices in MRI: Impact of number and arrangement of transmit channels,” *Magnetic Resonance in Medicine*, vol. 83, pp. 299–311, jan 2020.
- [47] N. Gudino, M. Sonmez, Z. Yao, T. Baig, S. Nielles-Vallespin, A. Z. Faranesh, R. J. Lederman, M. Martens, R. S. Balaban, M. S. Hansen, and M. A. Griswold, “Parallel transmit excitation at 1.5 T based on the minimization of a driving function for device heating,” *Medical Physics*, vol. 42, pp. 359–371, jan 2015.
- [48] D. J. Griffiths, “Introduction to Electrodynamics,” pp. 215–242, june 2017.

## Derivation of $B_{sct}$ equation

In Figure A.1, a segment of an infinitely long wire is illustrated in blue. The wire, spanning from point A to B, is carrying an electric current denoted by  $I$ . This Appendix is concerned with the derivation of the magnetic field at point P, resulting from the current flowing through the segment CD, which has a length of  $dl$  [48]. Point P is located at a distance  $R$  from the wire's center, denoted by O.

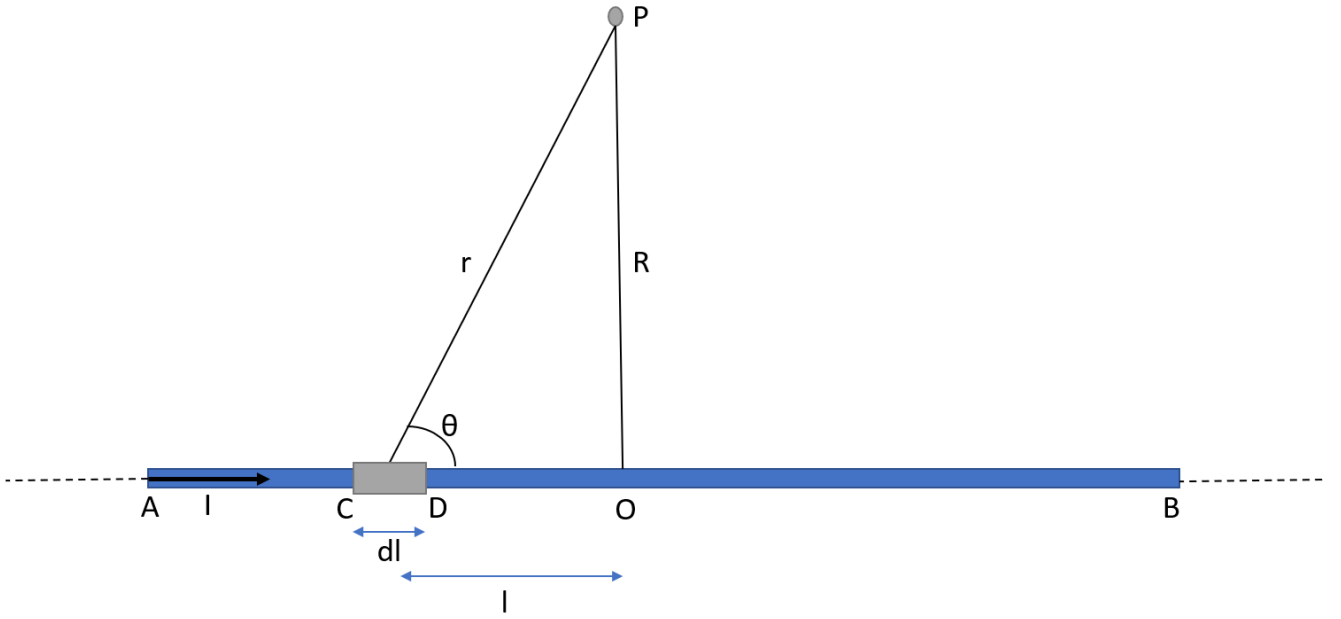


**Figure A.1:** A section of a infinitely long straight wire.

The Biot-Savart Law is a physical principle that characterizes the magnetic field produced by an electric current, and it is expressed mathematically as follows:

$$dB = \frac{\mu_0}{4\pi} \cdot \frac{I \cdot dl \cdot \sin\theta}{r^2} \quad (\text{A.1})$$

The magnetic field, denoted as  $B$ , at point P can be expressed as:

$$B_\phi = \int_{wire} dB \quad (\text{A.2})$$

$$B_\phi = \int_{wire} \frac{\mu_0}{4\pi} \cdot \frac{I \cdot dl \cdot \sin\theta}{r_P^2} = \frac{\mu_0 \cdot I}{4\pi} \int_{wire} \frac{\sin\theta}{r_P^2} dl \quad (\text{A.3})$$

This magnitude of the magnetic field of scattered by the wire is also called  $B_\phi$ . It should be noted that the magnetic field  $B$  exhibits a circular pattern around the wire, and the optimal method for its representation is in cylindrical coordinates. Concerning the infinitely long wire, the above Equation is integrated over the interval ranging from 0 to infinity, thereby resulting in the following expression:

$$\mathbf{B} = \frac{\mu_0 \cdot I}{2\pi} \int_0^\infty \frac{\sin\theta}{r_P^2} dl \cdot \hat{\phi} \quad (\text{A.4})$$

By employing trigonometric principles in Figure A.1, the following statements can be made:

$$r_P = \sqrt{l^2 + R^2} \quad (\text{A.5})$$

$$\sin\theta = \frac{R_P}{r_P} \quad (\text{A.6})$$

Equation A.5 and A.6 can be substituted in Equation A.4, yielding the following expression:

$$\mathbf{B} = \frac{\mu_0 \cdot I}{2\pi} \int_0^\infty \frac{R_P}{(l^2 + R_P^2)^{3/2}} dl \cdot \hat{\phi} \quad (\text{A.7})$$

By integrating this, the following outcome can be obtained:

$$\mathbf{B} = \frac{\mu_0 \cdot I}{2\pi} \left[ \frac{l}{R_P (l^2 + R_P^2)^{1/2}} \right]_0^\infty \cdot \hat{\phi} \quad (\text{A.8})$$

$$\mathbf{B} = \frac{\mu_0 \cdot I}{2\pi \cdot R_P} \cdot \hat{\phi} \quad (\text{A.9})$$

This Equation describes the magnitude of the magnetic field scattered by the wire, as observed at point P.

# Safety restrictions DBS lead

**Table B.1:** Conditional safety limits of Boston Scientific Cartesia Directional lead DB-2202-30.

Scan situation	Field strength (T)	Whole or Head SAR (W/kg)	$B_{1,rms}^+$ ( $\mu\text{T}$ )
Head transmit/ receive coil	1.5	$\text{SAR} \leq 0.1$	$B_{1,rms}^+ \leq 2.0$
Full body coil - isocenters above thoracic vertebra T12	1.5	$\text{SAR} \leq 0.1$	$B_{1,rms}^+ \leq 1.2$
Full body coil - isocenters at or below thoracic vertebra T12	1.5	$\text{SAR} \leq 0.1$	$B_{1,rms}^+ \leq 2.0$



# Additional information scan protocol

The predicted safety values calculated by the scanner are indicated in Table C.1. These values were measured during a measurement with head phantom 2. In addition, temperature measurements were performed during these sequences displayed in Figure C.1.

**Table C.1:** The predicted safety values of the sequences in the scan protocols.

Sequence	SAR value Whole body (%)	$B_{1,rms}^+$ ( $\mu T$ )	RF power (W)
Localizer 1	2.9	0.46	1.49
Localizer 2	3.2	0.46	1.64
Slice position	64	2.02	35.87
Pre-scan: calibration scan 1	0.4	0.17	0.21
Pre-scan: calibration scan 2	0.3	0.14	0.17
Pre-scan: IF mode (manual)	0.7	0.21	0.36
Pre-scan: IF mode ( $B_{1,inc}^+$ )	0.9	0.24	0.47

This Figure shows that all measurements required to calculate the IF mode are safe for the patient (less than 2°C elevation). Only the measurement that exceeds this safety standard is the T2\_TSE sequence used to determine slice position.

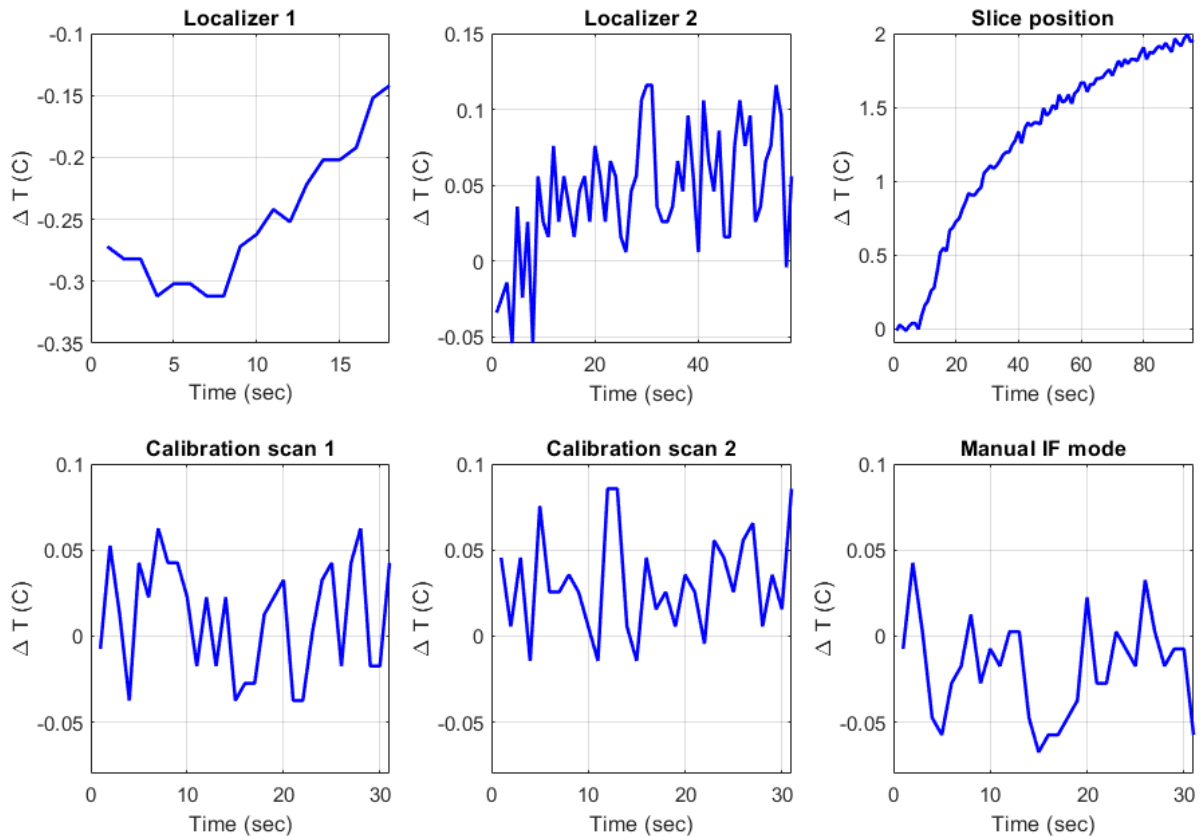


**Figure C.1:** The heating measured during six different sequences. The y-axis represents the temperature increase and the x-axis the time.



# Temperature rise in background

The temperature measurements of the probe placed in the background of the phantom are presented in Figure D.1. This measurement serves as a reference for the study. The results indicate that the maximum heating observed for the four different excitation patterns is similar.

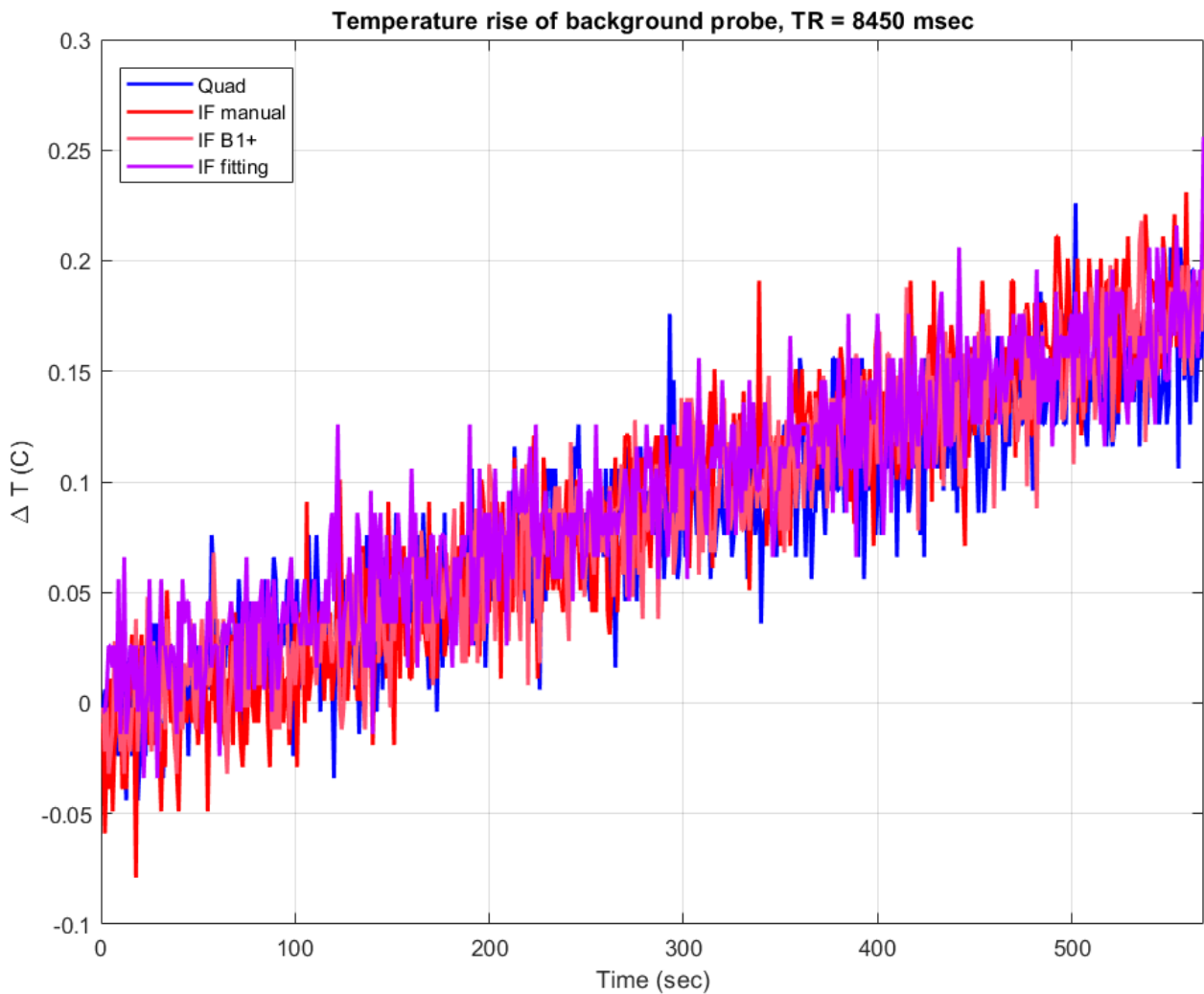


**Figure D.1:** The temperature rise of the background probe measured with four excitation patterns.